SUPPLEMENTAL INFORMATION

Supplemental Methods

Mouse studies

Hearts from 12-16 week old wild type C57/BL6 (Envigo, Horst, The Netherlands and Charles River Wilmington, MA, USA), $Cx43^{fl/fl}$ and $Cx43^{Cre\text{-}ER(T)/fl}$ mice (both kindly provided by Dr. R. Schulz, Justus-Liebig-Universität, Giessen, Germany; both transgenic strains have C57/BL6 background) were excised and subjected to enzymatic digestion (see below). Animals were housed in a licensed facility and handled in accordance with European Directive 2010/63/EU. Experimental methods were approved by the local ethical committees at Ghent University and New York University School of Medicine. Transgenic mice have been described in detail before (1-7). In short, in the $Cx43^{Cre\text{-}ER(T)/fl}$ mice one coding region of the Cx43 gene was replaced by a fusion construct of the Cre recombinase and a mutated version of the ligand binding domain of the human estrogen receptor (Cre-ER(T)), while the other allele was flanked by loxP sites. Both Cx43 alleles were flanked by loxP sites in $Cx43^{fl/fl}$ mice. Both transgenic strains show normal cardiac development to an adult stage. Daily intraperitoneal injection of 3 mg 4-hydroxytamoxifen (4-OHT; Sigma-Aldrich, Bornem, Belgium) dissolved in sunflower oil, for 5 consecutive days, induces Cre-ER(T) activity which progressively deletes the floxed Cx43 allele in adult $Cx43^{Cre\text{-}ER(T)/fl}$ mice. Hereby circumventing compensatory mechanisms during cardiac development and preventing perinatal death of Cx43-null mice due to right ventricular outflow tract obstruction (8). Experimental work was performed on day 11 after the first injection. 4-OHT-treated $Cx43^{fl/fl}$ mice were used as controls.

For cardiomyocyte isolation, mice were heparinized (Heparin sodium salt from porcine intestinal mucosa; Sigma-Aldrich, Bornem, Belgium) and sacrificed by cervical dislocation. Following thoracotomy, the heart was quickly excised and submerged in ice-cold Ca^{2+}-free isolation solution consisting of (in mmol/L): 130 NaCl, 5.6 KCl, 3.5 $MgCl_2$, 10 Glucose, 5 HEPES, 0.4 Na_2HPO_4, 20 Taurine and pH adjusted to 7.4 with NaOH. Subsequently, the aorta was cannulated using a blunt 24G needle, transferred to a Langendorff apparatus and perfused at a constant flow (~3 mL/min) and temperature (37°C) with Ca^{2+}-free isolation to wash out the remaining blood. Next, the heart was perfused with Ca^{2+}-free isolation solution containing collagenase (Type II, Worthington, Lakewood, New Jersey, USA), protease (Type XIV from *Streptomyces griseus*; Sigma-Aldrich, Bornem, Belgium) and additional 50 nmol/L of Ca^{2+} to activate the enzymatic activity. Bovine Serum Albumin (BSA; Sigma-Aldrich, Bornem, Belgium) was included during the enzymatic digestion to dilute the proteolytic activity and to attain optimal myocyte dissociation with improved cell viability. In the following step, the heart was removed from the perfusion system and the left ventricle was isolated from the rest of the heart, minced and incubated in the same enzymatic solution without protease for 5 minutes. All solutions were oxygenated during the isolation procedure. At the end, cells were dispersed by gentle agitation, filtered through a nylon mesh and 1 mg/mL BSA was added to the final cell suspension to stop enzymatic activity. Cardiomyocytes were centrifuged at low speed and resuspended in low-Ca^{2+} Tyrode solution consisting of (in mmol/L): 120 NaCl, 5.6 KCl, 5 $MgSO_4$, 0.2 $CaCl_2$, 5 Na-Pyruvate, 20 Glucose, 20 Taurine, 10 HEPES and pH adjusted to 7.4 with NaOH. Cell suspension was allowed to rest for 30 minutes before titrating $[Ca^{2+}]_o$ up to 1 mmol/L. Ca^{2+}-tolerant cells were stored at room temperature and used within 6 h after isolation.

DNA extraction and Polymerase Chain Reaction

DNA was extracted from mouse tail samples using the KAPA express kit (Sigma-Aldrich, Bornem, Belgium) and cDNA was amplified using the KAPA2G Fast Genotyping kit (Sigma-Aldrich, Bornem, Belgium) according to the manufacturer's instructions.

For primer sequences, see Supplemental Table 1. All primers were synthesized by Invitrogen (Ghent, Belgium). The PCR end-products were separated on a 1.5 % agarose gel and visualized with SYBR Safe DNA gel stain (Invitrogen, Ghent, Belgium).

Target	Primer name	Primer sequence
Fl	UMP	5' TCATGCCCGGCACAAGTGAGAC 3'
	UMPR	5' TCACCCCAAGCTGACTCAACCG 3'
Cre-ER(T)	Cre26	5' CCTGGAAAATGCTTCTGTCCG 3'
	Cre36	5' CAGGGTGTTATAAGCAATCCC 3'

Supplemental Table 1. *Primer sequences*

Pig studies

Healthy control pigs (Sus scrofa domesticus, Piétrain breed, 40-45 kg; Lovenjoel, Belgium) were housed and treated according to European Directive 2010/63/EU. Experimental protocols were approved by the in-house ethical committee (*Ethische Commissie Dierproeven*, KU Leuven).

Pig left ventricular cardiomyocytes were obtained as described previously (9). Pigs were heparinized and sacrificed under full anesthesia with an overdose of pentobarbital, after which the heart was quickly excised. Ventricular myocytes were enzymatically isolated from a wedge of the left ventricular free wall following

cannulation of a perfusing artery (left anterior descending artery or circumflex branch of the left coronary artery). The tissue was perfused with a constant flow (~4 mL/min) at 37°C. All solutions were oxygenated. First, the tissue was briefly perfused for 5 minutes with normal Tyrode to wash out the remaining blood (in mmol/L: NaCl 137, KCl 5.4, $MgCl_2$ 0.5, $CaCl_2$ 1.8, HEPES 11.8, glucose 10, pH 7.4 with NaOH), followed by 30 minutes perfusion with Ca^{2+}-free Tyrode's solution (in mmol/L: NaCl 130, KCl 5.4, HEPES 6, $MgSO_4$ 1.2, KH_2PO_4 1.2, glucose 20; pH 7.40 with NaOH). Next, the tissue was perfused with 1.4 mg/ml collagenase A (Roche, Switzerland) and 0.1 mg/ml protease (Type XIV from *Streptomyces griseus*; Sigma-Aldrich, Bornem, Belgium) in Ca^{2+}-free isolation solution. The enzyme solution was washed out for 15 minutes with a low Ca^{2+} Tyrode's solution (0.18 mmol/L $CaCl_2$). Subsequently, the digested midmyocardial layers were minced, filtered through a nylon mesh, and the cells resuspended in low Ca^{2+} Tyrode's solution. After 30 minutes, the solution was slowly replaced with normal Tyrode. Ca^{2+}-tolerant cells were stored at room temperature and used within 10 h after isolation.

Cx43 gene silencing

Silencing of Cx43 gene was performed by RNA interference as described previously (10). In short, acutely isolated cardiomyocyte suspension was centrifuged at 300 rpm for 5 min. The cell pellets containing both cardiomyocytes and fibroblasts were resuspended in Medium 199 (Sigma-Aldrich) supplemented with 10 % FBS, 10 U/mL penicillin and 10 µg/mL streptomycin. After 2-h incubation at 37 °C in 5 % CO_2, cardiomyocytes remained suspended in the medium while fibroblasts adhered to the bottom of the polystyrene flask. The fibroblast-depleted suspension was again collected and cultured at a density of 2×10^4 cells/cm^2 in a Petri dish (9.2 cm^2; TPP

Techno Plastic Products AG, Trasadingen, Switzerland) or glass coverslip (2.5 cm^2) coated in advance with natural mouse laminin (Invitrogen).

Cultured cardiomyocytes were transfected the following day with siRNA using DharmaFECT lipid reagent (Dharmacon, Thermo Fisher Scientific, Aalst, Belgium). Two siRNA probes targeting the porcine Cx43 gene *gja1* were synthesized and annealed by Eurogentec (Luik, Belgium) (Supplemental Table 2). Cultures transfected with scrambled sequence ($siCx43^{scr}$, Supplemental Table 2) or lipid reagent alone (MOCK) were used as negative controls. The transfection mixture was removed from the cultures after 24h treatment.

Peptide	Sense Sequence
$siCx43^{1}$	5′-GAAAGAGGAGGAACUCAAA-3′
$siCx43^{2}$	5'-ACUCGAUGCUGGCCAUGAA-3'
$siCx43^{scr}$	5′-AGAGAUACGAACAAGAGAG-3′

Supplemental Table 2. *siRNA probes*

Human studies

Single myocytes were enzymatically isolated from rejected donor hearts and explanted hearts. Experimental procedures were approved by the Ethical Committee of the University Hospital of Leuven with permit number S58824; as this is residual tissue no informed consent was necessary.

Human left ventricular cardiomyocytes were prepared with an adjusted protocol from Sipido et al. (11, 12).Hearts were collected in the operating room. Following explant, the heart was immediately placed in ice-cold cardioplegic Tyrode's solution (in mmol/L: NaCl 130, KCl 27, HEPES 6, $MgSO_4$ 1.2, KH_2PO_4 1.2, glucose 10; pH 7.40 with NaOH) and transported to the lab. A wedge of the left ventricular free wall with its perfusing

coronary artery was excised and the artery cannulated in cardioplegic solution. If possible the left anterior descending coronary was used, otherwise the left circumflex branch was used. After cannulation, the tissue wedge was perfused with constant flow (~4 mL/min at 37°C) with Ca^{2+} free Tyrode's solution for 30 minutes followed by enzyme perfusion for 40 minutes (collagenase A 1.4 mg/mL (Roche) and protease type XIV from *Streptomyces griseus* 0.1 mg/mL (Sigma-Aldrich) in Ca^{2+} free solution). The enzyme solution was washed out with low Ca^{2+} solution for 20 minutes. The digested midmyocardial layers were then dissected, minced, filtered and resuspended in low Ca^{2+} solution (0.18 mmol/L $CaCl_2$). After 30 minutes the low Ca^{2+} solution was slowly replaced with a normal Tyrode's solution containing 1.8 mmol/L $CaCl_2$. Cells were stored at room temperature and used within 6 h after isolation.

Whole-cell patch clamp

Isolated cardiac myocytes were placed in a recording bath and continuously perfused with normal Tyrode's solution at 37°C. Only rod-shaped cells with clear cross striations, and without spontaneous contractions or membrane blebs were used for experiments. Membrane currents and voltage were sampled in whole-cell voltage-clamp mode with an EPC 7 PLUS patch clamp amplifier (HEKA Elektronik, Germany; for mouse studies) and Axon Axopatch 200B (Axon Instruments/Molecular Devices, USA; for pig and human studies). Data were acquired at 4 kHz and digitized using a NI USB-6221 (National instruments, Austin, TX, USA) or Digidata 1440A (Axon instruments/Molecular Devices, San Jose, CA, USA) data acquisition device to WinFluor (John Dempster, Strathclyde University) or Clampex 10.2 acquisition software (Axon instruments/Molecular Devices, San Jose, CA, USA). All currents were filtered at 1 kHz (7-pole Besselfilter). Amplifier gain was carefully adjusted to allow

simultaneous sampling of macroscopic and microscopic currents of interest with ideal resolution.

The composition of normal Tyrode's solution used for recording of membrane currents and membrane voltage was: (in mmol/L) NaCl 137, NaAspartate 2, KCl 5.4, $MgCl_2$ 0.5, $CaCl_2$ 1 for mouse and 1.8 for pig and human, HEPES 11.8, glucose 10 (pH 7.4 with NaOH). Patch pipettes (2-3 MΩ) were filled with standard pipette solution containing: (in mmol/L) KAspartate 120, KCl 20, $MgCl_2$ 0.5, MgATP 5.0, HEPES 10, NaCl 10, K_5fluo-4 0.05 (pH 7.20 with KOH). $[Ca^{2+}]_i$ dependence was assessed by adding 10 mmol/L BAPTA to the pipette solution (Supplemental Figure 3). In a subset of experiments, stably buffered $[Ca^{2+}]_i$ was imposed by adding 5 mmol/L EGTA as a Ca^{2+} buffer and calculating the amount of Ca^{2+} to be added (by using Webmax Calculator, https://somapp.ucdmc.ucdavis.edu/pharmacology/bers/maxchelator/webmaxc/webmaxcS.htm) in order to obtain solutions with $[Ca^{2+}]_i$ of 50, 250, 500 or 1000 nmol/L. Cells were stimulated to steady-state by depolarizing steps (25 ms for mouse (mimicking the short action potential) and 200 ms for pig and human) from –70 to +10 mV at 1 Hz for 2 minutes, followed by fast caffeine application (10 mmol/L for 8 s) at -70 mV (Figure 1A). Addition of the 2 min stimulation train prevented channel rundown during the recording (Supplemental Figure 2A). Alternatively, in cells that exhibited unitary current activity, the stimulation period was followed by a 15 s resting period at -70 mV to allow diastolic Ca^{2+} release from the SR and resulting currents (Figure 6A). For study of voltage dependence and channel selectivity, recordings were performed following 15 pulses pacing at 1 Hz and under conditions of K^+-channel blockade or exclusion of major charge-carrying ions. In a subset of experiments, protocols were repeated at different frequencies and in the presence or absence of ISO (1 µmol/L for mouse

studies and 10 nmol/L for pig and human studies) (Figure 2 and 3). Delayed afterdepolarizations (DADs) were recorded in current-clamp mode following a 2 minute stimulation period in voltage-clamp mode. Different conditions were applied in random order to minimize time-dependent changes following isolation.

$[Ca^{2+}]_i$ imaging

$[Ca^{2+}]_i$ was reported making use of fluo-4 loaded into the cell through the patch pipette in order to avoid compartmentalization, bleaching and loss of dye. Proper and stable dye loading was ensured before initiating experiments. For mouse experiments, widefield fluorescence was simultaneously acquired during electrophysiology using an inverted epifluorescence microscope (Motic AE31 Trinocular) with a custom-built imaging module. Dye was excited with a Mercury arc lamp (Nikon) at 475±35 nm. The dichroic mirror under the objective (Nikon x40/1.3 oil immersion objective lens) was centered at 510 nm. Fluo-4 fluorescence was sampled at 535±35 nm using a CCD camera (CoolSnap HQ2; Photometrics, AZ, USA) at 100 Hz. For pig and human experiments, confocal line scan images were simultaneously recorded during electrophysiology using a Zeiss Axiovert 100M inverted microscope with a x40/1.3 oil-immersion objective and a Zeiss LSM 510 confocal laser point-scanning system. Fluo-4 was excited at 488 nm with a 25 mW argon laser. Cells were scanned along the longitudinal axis, orthogonal to the Z lines, avoiding scanning through nuclei. Line scans were recorded at 650 Hz with a pixel size of 0.2–0.3 µm. The fluorescence signals obtained with fluo-4 were corrected for the background fluorescence recorded after seal formation, and normalized for baseline values at rest before stimulation.

Macropatch recording

A subset of electrophysiological recordings was performed in the macropatch cell-attached configuration, as described previously (13-15). Pipette resistance was maintained within the range of 1.9 to 2.1 MΩ, to facilitate reproducibility between experiments. Only recordings obtained under seal resistances higher than 2 GΩ were used in this study. Recording pipettes were filled with Tyrode's solution with K^+ replaced by Cs^+, TEA^+ and Ba^{2+}. Cells were maintained in a solution containing 0.33 mM NaH_2PO_4, 5 mM HEPES, 1.8 mM $CaCl_2$ and 140 mM KCl, pH 7.4 with KOH, thus depolarizing the membrane potential to a value estimated to be near zero. In this configuration (recording electrode in the extracellular space), voltage command pulses of negative polarity were necessary to depolarize the inside of the cell, and the elicited currents were positive when inward. Following the standard convention, membrane potential is reported as the difference between the inside of the cell, and a distant ground in the bath, and current direction and polarity is reported as if recorded from the cell interior. Recordings were obtained either from the end of the cell, in the area previously occupied by the ID, or from the lateral membrane (LM) section of the cell. Recordings in cell pairs were obtained from the site of cell-cell contact. Cells were stepped to different voltages from a holding potential of -70 mV. Caffeine and TAT-conjugated Cx mimetic peptides were added to the bath solution when applicable. Currents were sampled at 10 kHz and low-pass filtered at 1 kHz (7-pole Besselfilter). Amplifier gain was carefully adjusted to allow single channel recording with ideal resolution.

Scanning ion conductance microscopy and super-resolution patch clamp

Scanning ion conductance microscopy (SICM) is a non-contact scanning probe super-resolution (<20 nm) technique that produces a 3-dimensional topographic image of the

surface of living cells based on the principle that the ion flow through the tip of a nanopipette is determined by the distance to the sample surface (for a detailed description of the technique, see Bhargava et al. (16)). After surface scanning, nanopipette was clipped in a controlled manner and patch clamping was performed at a chosen location just distally from the last Z-groove. Recording solutions and current sampling and filtering were identical to cell-attached macropatch technique. Only recordings obtained under seal resistances higher than 5 GΩ were used in this study.

Peptide tools

Synthetic Cx mimetic peptides (Supplemental Table 3) used in this study were all obtained from Pepnome (Hong Kong, China). For whole-cell recording, non-TAT-conjugated peptides were all added to the pipette solution in a concentration of 100 µmol/L. Except ^{10}Panx1, which was pre-incubated at 200 µmol/L for 30 minutes. For macropatch experiments, ^{10}Panx1 was included in the pipette solution at 200 µmol/L. TAT-conjugated peptides were all added to the bath solution in a concentration of 80 µmol/L. The identity of the peptides was confirmed by mass spectrometry and purity was ≥ 90 %. Proper loading of peptides included in the patch pipette and action of peptides was ensured by waiting sufficient time before start of protocols. Different interventions were tested in random order to minimize time-dependent changes in channel expression, distribution and function following cell isolation.

Peptide	Sequence
Gap19	^{128}KQIEIKKFK^{136}
Gap19^{I130A}	^{128}KQAEIKKFK^{136}
CT9	^{374}RPRPDDLEI^{382}
^{10}Panx1	^{74}WRQAAFVDSY^{83}
TAT-Gap19	YGRKKRRQRRR-^{128}KQIEIKKFK^{136}
TAT-Gap19^{I130A}	YGRKKRRQRRR-^{128}KQAEIKKFK^{136}
TAT-CT9	YGRKKRRQRRR-^{374}RPRPDDLEI^{382}

Supplemental Table 3. *Peptide sequences*

Analysis of membrane currents

For single channel and Na^+/Ca^{2+} exchange (NCX) current analysis, all qualitative traces were included in the analysis. Complex electrophysiological signals containing NCX and unitary currents were automatically separated and analyzed using a novel cross-correlation and threshold detection algorithm written in python using the packages numpy, scipy, pyqt and matplotlib. For unitary currents, threshold was set at five times standard deviation of noise distribution and allows reliable detection of ~99% of unitary current events (17). Elementary current transitions (Δi) were fit by an error function and unitary conductances were calculated as: $\gamma = \Delta i / V_m$. From these data, we constructed all-event transition conductance histograms. Distributions were fit by probability density functions assuming independent channel opening (18, 19). Event probability was calculated as the summed open time divided by the duration of the time window of interest. Single-channel open probability was calculated for recordings in cell-attached configuration by dividing event probability by the amount of channels in the patch as estimated by the level of stacked events. Availability is defined as the fraction of sweeps containing at least 1 channel opening. Time to first event was determined as time from start of NCX current to first unitary current transition. SR Ca^{2+} content was measured by integrating the inward NCX current during fast caffeine application (10 mmol/L).

Confocal microscopy

Freshly isolated left ventricular cardiomyocytes were fixed with 2% paraformaldehyde (PFA) for 15 minutes. Subsequently, cells were washed 3 times and background fluorescence was quenched with 50 mM glycine, cells permeabilized using 0.2% Triton

X-100 and blocked with 10% goat serum and 1% BSA in PBS (blocking buffer) for 1 hour at room temperature. Cells were washed three times between every step. Primary antibody (rabbit Cx43, C6219, 1:500; Sigma-Aldrich, Bornem, Belgium) diluted in blocking buffer was incubated overnight at 4°C. Cells were washed 3 times and incubated with secondary antibody (Alexa Fluor 488, A-11008, 1:200; Life Technologies) in blocking buffer for 1 hour at room temperature. Next, cells were washed three times and incubated with Phalloidin-Rhodamin (1:200; R415, Life Technologies) in blocking buffer for 45 minutes at room temperature. Cells were then washed 3 times before imaging. Confocal micrographs were acquired with a commercially available Leica system (TCS SP8x) using x63 objective within respective excitation-emission spectra. Z-sections were taken every 0.5 µm.

Super-resolution fluorescence microscopy

22-squared coverslips (Fisherbrand) were coated with 10 µg/mL laminin (BD Biosciences) for 30 min. Isolated adult left ventricular cardiomyocytes were plated on the coverslips and allowed to attach to the surface for 45 min at 37 °C. Cells were fixed with 4% PFA in PBS for 10 min, washed 3 times with PBS and left in PBS until further processing for immunostaining. Samples were permeabilized with 0.1% Triton in PBS for 10 min at room temperature. Blocking was done with PBS containing 2% bovine serum albumin, 2% glycine, and 0.2% gelatin for 30 min. Primary antibodies rabbit anti-Cx43 (1:200, AB1728, Millipore), mouse anti-Cx43 (1:100, clone 4E6.2, MAB3067, Millipore), rabbit anti-NCX (1:25, sc-32881, Santa Cruz Biotechnology), rabbit anti-$Ca_V1.2$ (1:200, ACC-003, Alomone), anti-phospholamban (1:100, sc-393990, Santa Cruz Biotechnology), rabbit anti-JPH2 (1:50, 40-5300, Thermofisher), anti-caveolin-3 (1:100, 610421, BD Bioscience),

mouse anti-α-actinin (1:100, A7811, Sigma-Aldrich) and mouse anti-RyR2 (1:100, MA3-916, Thermofisher) were diluted in blocking solution and incubated for 1 h at room temperature. Primary antibodies were washed with PBS and secondary antibodies anti-mouse or anti-rabbit Alexa Fluor 647 (1:10000, A-21235 or A-21244, Life Technologies), anti-mouse or anti-rabbit Alexa Fluor 568 (1:10000, A-11004 or A-11011, Life Technologies) and anti-mouse Alexa Fluor 488 (1:5000, A-11008, Life Technologies) were incubated for 30 min at room temperature. For triple staining, mouse anti-RyR2 (MA3-916, Thermofisher) directly conjugated to Alexa Fluor 647 was additionally used (1:100, A20186, Thermofisher). For super-resolution fluorescence imaging, coverslips were mounted on slides with imaging buffer: 200 mM mercaptoethylamine and an oxygen scavenging system: 0.4 mg/ml glucose oxidase, 0.02 mg/ml catalase and 10% (wt/wt) glucose. Samples were imaged in a custom-built microscope set up equipped with a Leica DM3000 microscope, a 556 nm and 640 laser (OEM Laser Systems) and an HCX PL APO ×100 NA = 1.47 OIL CORR TIRF objective. Total internal reflection fluorescence or highly inclined illumination modes were used to excite the samples and improve signal-to-noise ratio. A Prime Scientific CMOS camera (Photometrics) was used to image different color movies containing 2000 frames. Each movie was reconstructed at 20 nm, processed with a smoothing filter and adjusted for brightness and contrast using automated MATLAB and ImageJ routines. Cluster detection (cluster size and density – defined as the number of clusters per unit of area) and distance analysis was performed using automated ImageJ and Python routines. Analysis of the number of RyR units per cluster was achieved with the density-based clustering algorithm DBSCAN, which groups together points that are closely packed together (with many nearby neighbors), marking as outliers points that lie alone in low-density regions

(nearest neighbors too far away). DBSCAN uses two input parameters—Eps and MinPts—and determines that a point is in a cluster if at least MinPts points are within a distance of Eps. We used an Eps value of 50 nm and a Minpts of 10 for DBSCAN analysis (20).

Single hemichannel modeling

Cx43 hexamers were generated using SWISS-MODEL (21) and SymmDock (22) based on murine Cx43 sequence (UniProtKB P23242). Hexagonal grids of Cx43 hemichannels with variable interspacing were used to estimate number of Cx43 hemichannels per dyad.

Electron Microscopy

Electron Microscopy Sample Preparation

Mice were anesthetized with sodium pentobarbital, perfused with 4% paraformaldehyde in PBS and then euthanized by excision of the heart. The perfused heart was cut into 1 mm^3 and placed in a fixative solution containing 2% paraformaldehyde and 2.5% glutaraldehyde in phosphate buffer (PB, pH 7.2). Fixed mouse heart was further processed with modified OTTO (23), and embedded in Durcupan. In brief, the heart tissue was washed with 0.1 mol/L PB, post fixed in 2% OsO_4 / 1.5% potassium ferrocyanide for 1.5 h at room temperature, then stained with freshly made 1% tannic acid (EMS) in PB for two consecutive steps with 2 hours each step at 4°C to allow for additional staining. The tissue was then washed in ddH_2O, placed in 2% aqueous OsO_4 for 40 min at room temperature, and *en bloc* stained in 1% aqueous uranyl acetate at 4°C overnight. The tissues were then washed with ddH_2O, dehydrated in a series of ethanol solutions (30, 50, 70, 85, 95, 100, 100%; 10

min each, on ice) and replaced with ice-cold dry acetone for 10 min, followed by 10 min in acetone at room temperature. The sample was gradually equilibrated with Durcupan ACM Araldite embedding resin (Electron Microscopy Sciences, EMS, PA) and embedded in fresh made 100% Durcupan.

Serial Block-Face Scanning Electron Microscopy (SBF-SEM)

The sample block was trimmed and thin sections were cut on slot grids to identify the area of interest. The sample block was then mounted on an aluminum specimen pin (Gatan, Pleasanton, CA) using silver conductive epoxy (Ted Pella Inc.) to electrically ground the tissue block. The specimen was trimmed again with pyramid shape and coated with a thin layer of gold/palladium (Denton Vacuum DESK V sputter coater, Denton Vacuum, LLC., NJ, USA). Serial block face imaging was performed using Gatan OnPoint BSE detector in a Zeiss GEMINI 300 VP FESEM equipped with a Gatan 3View automatic microtome unit. The system was set to cut sections with 100 nm thickness, imaged with gas injection setting at 65% (3.9E-03 mbar) with Focus Charge Compensation to reduce the charge, and images were recorded after each round of section from the block face using the SEM beam at 1.2 keV with a dwell time of 1.0 µs/pixel. Each frame is 20 x 25 µm with pixel size of 2 nm. Data acquisition occurred in an automated way using the Auto Slice and View G3 software. A stack of 150 slices was aligned and assembled using ImageJ. A volume of roughly 20x25x15 μm^3 dimensions was obtained from the tissue block.

Cell culture

HEK cells overexpressing RyR2 under the control of a tetracycline-inducible promoter (HEK RyR2 cells) were produced as described in (24) and kindly provided by the group

of Dr. S.R. Wayne Chen. HEK RyR2 cells were cultured in Dulbecco's modified eagle medium (DMEM) supplemented with 10% serum, penicillin/streptomycin (100 IU/ml), glutamax (2 mmol/L) at 37°C with 5% CO_2. One day after plating the medium was replaced with medium containing 1 µg/ml tetracycline. Cells were used for intracellular Ca^{2+} measurements after 24 hours.

Fura2-AM intracellular Ca^{2+} measurements

HEK RyR2 cells seeded in clear bottom black 96 well plates (Greiner), were loaded for 30 min at room temperature with 1.25 µmol/L Fura-2AM in modified Krebs solution (containing (in mmol/L) NaCl 150, KCl 5.9, 1.2 $MgCl_2$ 1.2, HEPES 11.6, glucose 11.5 and $CaCl_2$ 1.5 (pH 7.3 with NaOH). After washing the cells twice with modified Krebs solution, de-esterification was performed by incubating in Fura-2AM free modified Krebs solution for 30 min at room temperature. Intracellular Ca^{2+} measurements were performed using a multi-mode microplate reader Flexstation 3 (Molecular Devices) by alternately excitation at 340 and 380 nm and measuring emitted fluorescence at 510 nm. Additions (peptides, EGTA and caffeine) were performed as indicated in the figures at the indicated concentrations. When pre-treatment was necessary the peptides were included during the de-esterification step. All traces are shown as the ratio of measured emission of Fura-2 (F_{340}/F_{380}). Experiments were repeated 5 times independently measuring each condition in duplicate on each day.

Western blot analysis

Following enzymatic digestion, mouse atria and right ventricle were snap frozen in liquid nitrogen and stored at -80°C. Tissue and cell lysates were prepared by treating the samples with RIPA buffer (25 mmol/L Tris, 50 mmol/L NaCl, 0.5% NP-40, 0.5%

deoxycholate, 0.1% SDS, 5.5% β-glycerolphosphate, 1 mmol/L dithiothreitol, 15 µL/mL protease inhibitor cocktail (Sigma-Aldrich, Bornem, Belgium), 20 µL/mL of phosphatase inhibitor cocktail (Sigma-Aldrich, Bornem, Belgium) and 20 µL/mL mini EDTA-free protease inhibitor cocktail), homogenization and sonication. Protein concentration was determined with a Biorad DC protein assay kit and absorbance was measured with a 590 nm long-pass filter. Proteins were separated by electrophoresis on a 4-12% Bis-Tris gel (Invitrogen, Ghent, Belgium) and transferred to a nitrocellulose membrane (GE Healthcare, Diegem, Belgium). Blots were probed with primary antibody (1:5000 rabbit anti-Cx43 (C6219, Sigma), 1:250 rabbit anti-Panx1 (MA5-35664, Invitrogen), 1:250 mouse anti-polycystin-2 (sc-28331, Santa Cruz; kindly provided by Dr. J-P Decuypere, KU Leuven, Belgium) or 1:500 rabbit anti-PKD2L2 (OSP00010W, Thermofisher), followed by alkaline phosphatase conjugated goat anti-rabbit IgG (1:4000; A3687, Sigma-Aldrich, Bornem, Belgium) or HorseRadish Peroxidase (HRP) conjugated goat anti-rabbit or anti-mouse IgG (1:5000; sc-2004 or sc-2005, Santa Cruz Biotechnology, Heidelberg, Germany) and detection was performed with nitro blue tetrazolium/5-bromo-4-chloro-3-indolyl phosphate reagent (Invitrogen, Ghent, Belgium) or chemiluminescence respectively. Blots were treated with SYPRO® Ruby protein blot stain (Molecular Probes, Ghent, Belgium) or 1:1000 mouse anti-vinculin (V9131, Sigma-Aldrich, Bornem, Belgium) to verify loading.

Mathematical framework

Electrical effect of hemichannel opening

We determined the electrical impact of hemichannel opening making use of a membrane equivalent scheme (Supplemental Figure 1).

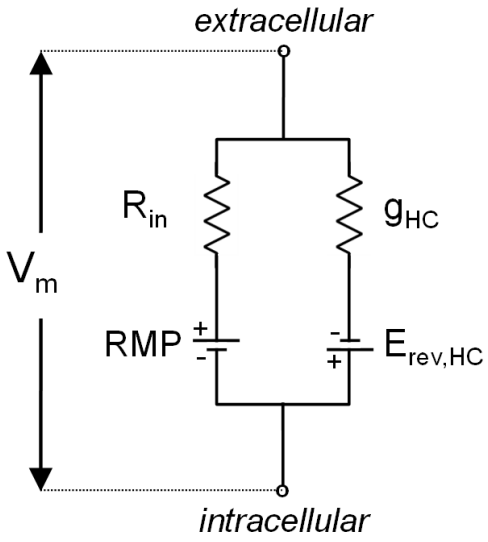

Supplemental Figure 1. Electrical equivalent scheme of a hemichannel in the sarcolemma. Two current paths are shown: the left arm contains a battery generating the resting membrane potential (RMP = -70 mV) in series with the cell input resistance (R_{in} = 94.92 ± 9.76 MΩ, N/n_{mouse} = 23/75, in line with reported ~40-100 MΩ in rodent ventricular cardiomyocytes (25-29); at resting V_m the main contributor to R_{in} is I_{K1} (30)). The right arm is composed of a hemichannel resistance (conductance g_{HC} of 227 ± 7pS, N/n_{mouse} = 90/281, 37°C) in series with a battery that has zero reversal potential ($E_{rev,HC}$ = 0 mV).

Application of Kirchhoff's junction and loop rules allowed to calculate the voltage drop over the cardiomyocyte input resistance (R_{in}) as $\Delta V_m = -V_m \cdot R_{in}/(R_{in} + 1/g_{HC})$, yielding a 1.48 mV depolarizing shift from -70 mV per hemichannel using the data given in the legend (Supplemental Figure 1). We verified this estimate by including a single human hemichannel with 228.1 ± 4.1 pS conductance (N/n_{NF} = 20/64) into two computational models of human ventricular cardiomyocyte electrophysiology: TNNP04 (31) and ORd (32), which resulted in 1.75 mV depolarization per hemichannel. We took an average of 1.6 mV depolarization per hemichannel taking into account the two distinct approaches. Stacked hemichannel openings will result in the summing of these depolarizing potentials.

Ca^{2+} current through a single hemichannel

441 At -70 mV, the current through a single hemichannel is -15.9 pA (inward current) in
442 mouse cardiomyocytes (37°C), which is carried by several ionic components including
443 Na^+, Ca^{2+}, K^+, Cl^- and Aspartate (Asp^-) as the main potential contributors.
444
445 To determine the fraction of the hemichannel current carried by Ca^{2+}, we first
446 considered to use a Goldman-Hodgkin-Katz based approach to calculate P_{Ca}/P_{Na} (33,
447 34) based on the observed shift in reversal potential (E_{rev}) of ~9.5 mV upon increasing
448 extracellular Ca^{2+} from 1 to 5 mM (Figure 1). However, such estimates would only be
449 valid at E_{rev} where the net current flow equals zero, but not at -70 mV that was used in
450 all present experiments. As a result, we determined the Ca^{2+} current ($I_{Ca,HC}$) relative to
451 the Na^+ current ($I_{Na,HC}$) using an alternative approach that was based on the ratio of
452 the respective steady state electrodiffusion flux equations for these ions (35):

453
$$\frac{I_{Ca,HC}}{I_{Na,HC}} = \frac{z_{Ca}\, D_{Ca}\, (\Delta C_{Ca} + z_{Ca}\, \bar{C}_{Ca} \frac{F}{RT}\, V_m)}{z_{Na}\, D_{Na}\, (\Delta C_{Na} + z_{Na}\, \bar{C}_{Na} \frac{F}{RT}\, V_m)} \quad (1)$$

454 with aqueous diffusion constants D_{Ca} and D_{Na} of 642 and 540 µm²/s (37°C) determined
455 under standardized conditions (617 and 519 µm²/s respectively at 25°C (36)), z_{Ca} and
456 z_{Na} as corresponding valences, ΔC_{Ca} and ΔC_{Na} as transmembrane concentration
457 differences, and $\bar{C}_{Ca}$ and $\bar{C}_{Na}$ average concentrations in the pore (taken as half
458 between outside and inside). This yields a $I_{Ca,HC}/I_{Na,HC}$ ratio of ~0.057, i.e. the Ca^{2+}
459 current is ~5.7% of Na^+ current. We next estimated the contribution of K^+, Cl^- and Asp^-
460 based on their driving forces (V_m - E_{Nernst}; Supplemental Table 4) and the hemichannel
461 conductance.
462

Ion	**E_{Nernst} (mV)**	**V_m - E_{Nernst} (mV)** (V_m = -70 mV)
Na^+	71.5	-141.5
Ca^{2+}	132.3	-202.3

K^+	-87.8	17.8
Cl^-	-41.3	-28.7
Asp^-	109.4	-179.4

Supplemental Table 4. Nernst potentials and driving forces (37°C)

The Cl^- current was corrected taking into account a P_{Cl}/P_K ratio of 0.13 as reported by Wang & Veenstra (37). Correction for Asp^-, was based on a glutamate permeability of 1.4 times less than the Cl^- permeability (37). The Ca^{2+} current was then calculated from the summed Na^+, K^+, Cl^- and Asp^- current contributions. The Ca^{2+} over Na^+ ratio ($I_{Ca,HC}/I_{Na,HC}$ = ~0.057; see above), allowed to express the equation in terms of Ca^{2+} current ($I_{Ca,HC}$), yielding ~0.84 pA per hemichannel for 1 mM extracellular Ca^{2+} (mice experiments). For the pig and human experiments, extracellular Ca^{2+} was 1.8 mM, which gave a hemichannel Ca^{2+} current of ~1.46 pA (all values at V_m = -70 mV and 37 °C). Based on this estimate, we explored the impact of hemichannel Ca^{2+} currents in a range of 0 to 3 pA on hemichannel-dyad microdomain Ca^{2+} elevation and its consequent effects on NCX current and Ca^{2+} waves (Figure 9).

Hemichannel associated Ca^{2+} elevation

For assessing the impact of hemichannel associated Ca^{2+} entry, we constructed a cell model with 2 separate compartments: a subsarcolemmal space interfacing with dyads at the perinexal microdomain and a cytoplasmic compartment with dyads and myofibrils deeper inside the cell. Mathematical parameters are summarized in Supplemental Table 5. Cytoplasmic and microdomain geometry were obtained from the mouse experiments.

Ca^{2+} entry (J_{HC}) through a single Cx43 hemichannel was calculated as (38-40):

$$J_{HC} = \frac{\mathrm{I}_{Ca,HC}}{z_{Ca}F} \quad (2)$$

The consequent whole-cell [Ca^{2+}] increase is provided by dividing hemichannel-associated Ca^{2+} entry by Ca^{2+}-accessible cytoplasmic volume (V_{acc}) (41-43):

$$[Ca^{2+}] = \frac{J_{HC}\tau_{o,HC}}{V_{acc}} \quad (3)$$

For calculation of microdomain-associated Ca^{2+}, we incorporated geometric approximations of the dyad and treated the channel as a point source from which Ca^{2+} diffuses away with hemispherical contours of equal concentration (44). The concentration of Ca^{2+} at distance r from the channel then calculates as:

$$[Ca^{2+}] = \frac{J_{HC}\tau_{o,HC}}{2\pi r_{PN} D_{sub}} \quad (4)$$

where J_{HC} is Ca^{2+} influx through a single hemichannel, r_{PN} is the thickness of the dyad at the perinexal microdomain and D_{sub} is the Ca^{2+} diffusion constant in the subsarcolemmal compartment.

In the subsarcolemmal space, Ca^{2+} diffuses and binds to stationary (phospholipids, SERCA) and mobile (calmodulin, ATP, fluo-4) Ca^{2+} buffers. In the cytoplasm, stationary buffers additionally include troponin C and myosin. Ca^{2+} buffering in both compartments was based on previously published values (summarized in Supplemental Table 5) and the relationship between total and free Ca^{2+} ($[Ca^{2+}]_{total}$ and $[Ca^{2+}]_i$ respectively) is provided by the following equation (45-48):

$$[Ca^{2+}]_{total} = a + \sum B_{max,i} \frac{[Ca^{2+}]_i}{K_{d,i} + [Ca^{2+}]_i} \quad (5)$$

where ‘a’ is an offset because the relationship cannot be determined for values of $[Ca^{2+}]_i$ below the resting level, $B_{max,i}$ is the total concentration of buffer ‘i’ and $K_{d,i}$ is the concentration of Ca^{2+} at which half of the buffer ‘i’ is occupied by Ca^{2+}.

NCX current (I_{NCX}) activated by hemichannel opening was calculated as (49-52):

$$I_{NCX} = \frac{FV_{dyad,PN}}{C_m} J_{NCX} \quad (6)$$

where $V_{dyad,PN}$ is dyadic volume at the perinexus, C_m is membrane capacitance and J_{NCX} is Na^+-Ca^{2+} exchange flux.

$$J_{NCX} = g_{NCX} A_{NCX} \frac{e^{\varepsilon VF/RT}[Na^+]_i^3[Ca^{2+}]_o - e^{\frac{(\varepsilon-1)VF}{RT}}[Na^+]_o^3[Ca^{2+}]_i}{(1 + k_{sat} e^{(\varepsilon-1)VF/RT})H} \quad (7)$$

where

$$H = K_{m,Cao}[Na^+]_i^3 + K_{m,Nao}^3[Ca^{2+}]_i \left(1 + \frac{[Ca^{2+}]_i}{K_{m,Cai}}\right) + K_{m,Cai}[Na^+]_o^3 \left(1 + \frac{[Na^+]_i^3}{K_{m,Nai}^3}\right)$$

$$+ [Na^+]_i^3[Ca^{2+}]_o + [Na^+]_o^3[Ca^{2+}]_i \quad (8)$$

and

$$A_{NCX} = \frac{1}{1 + \left(\frac{K_{mCaAct}}{[Ca^{2+}]_i}\right)^{n_{Hill}}} \quad (9)$$

Integration of this NCX current over the time window of hemichannel opening activity yields the NCX charge transfer provoked by hemichannel Ca^{2+} entry.

Hemichannel associated Ca^{2+} induced SR Ca^{2+} release

We adapted the method described by Cannell et al. to assess activation of RyRs due to hemichannel Ca^{2+} entry at the perinexal microdomain (53), with the probability of activation calculated as:

$$P_a = k_{on}[Ca^{2+}]_i C^* \quad (10)$$

where P_a is the activation probability, k_{on} is the RyR "on" rate and C* is the fraction of RyR available to open. C* is calculated from the expression:

$$C^* = \frac{k_{on}}{k_{on} + 2k_{off}} \quad (11)$$

where k_{off} is the RyR "off" rate.

The effect of RyR clustering is described by:

$$P_c = 1 - (1 - P_a)^{\beta_{PN}} \quad (12)$$

where P_c is the cluster activation probability and β_{PN} the number of RyRs in a cluster at the perinexus.

Ca^{2+} spark amplitude is provided by the following equations:

$$J_{spark} = \frac{\beta_{PN} I_{RyR}}{z_{Ca} F} \quad (13)$$

$$[Ca^{2+}] = \frac{J_{spark}}{2\pi r_{PN} D_{sub}} \quad (14)$$

The probability of a Ca^{2+} spark propagating from an activated RyR cluster to the next cluster at distance r_{myo} is described by the following equations (54):

$$[Ca^{2+}] = \frac{J_{spark}}{2\pi r_{myo} D_{cyto}} \quad (15)$$

$$P_a = k_{on}[Ca^{2+}]_i C^* \quad (16)$$

$$P_c = 1 - (1 - P_a)^{\beta_{myo}} \quad (17)$$

Parameter	Definition	Value	Reference
Cell geometry			
R	Cell width	20.6 µm	Experiment
L	Cell length	100.5 µm	
H	Cell height	14.2 µm	
S	Cell surface	7580 µm²	Estimate
C_m	Membrane capacitance	2 µF/cm²	(31)
V_{cell}	Cell volume	29.4 pL	Estimate
V_{acc}	Cytoplasmic volume accessible by Ca^{2+}	10.6 pL	
Microdomain geometry			
r_{PN}	Thickness of the subsarcolemmal space at the perinexus	9.8 nm	Experiment
$V_{dyad,PN}$	Dyadic volume at the perinexus	0.019 µm³	Estimate
$r_{myo,trans}$	Nearest RyR cluster edge distance transverse	0.56 µm	Experiment
$r_{myo,long}$	Nearest RyR cluster edge distance longitudinal	1.25 µm	

l_{myo}	Thickness of the dyad at the sarcomeres	11.08 nm	
$V_{dyad,myo}$	Dyadic volume at the sarcomeres	0.024 µm³	Estimate
Ion concentrations and temperature			
$[Na^+]_i$	Cytoplasmic Na^+ concentration	10 mmol/L	Experiment
$[Na^+]_o$	External Na^+ concentration	144.9 mmol/L	
$[K^+]_i$	Cytoplasmic K^+ concentration	144mmol/L	
$[K^+]_o$	External K^+ concentration	5.4 mmol/L	
$[Ca^{2+}]_o$	External Ca^{2+} concentration	1 or 1.8 mmol/L	
T	Temperature	310 K	
Ca^{2+} buffer concentrations			
$B_{max,TC}$	Cytoplasmic concentration of Troponin C (Mg) buffer	140 µmol/L	(46)
$B_{max,SERCA}$	Cytoplasmic concentration of SERCA buffer	47 µmol/L	
$B_{max,CALM}$	Cytoplasmic concentration of Calmodulin buffer	24 µmol/L	
$B_{max,phosphoL}$	Cytoplasmic concentration of phospholipid (low) buffer	42 µmol/L	
$B_{max,phosphoH}$	Cytoplasmic concentration of phospholipid (high) buffer	15 µmol/L	
$B_{max,myosin}$	Cytoplasmic concentration of myosin buffer	140 µmol/L	
$B_{max,ATP}$	Cytoplasmic concentration of ATP buffer	5 mmol/L	Experiment
$B_{max,FLUO}$	Cytoplasmic concentration of Fluo-4 buffer	50 µmol/L	
Ca^{2+} buffer dissociation constants			
$K_{d,TC}$	Dissociation constant for Troponin C (Mg) buffer	0.02 µmol/L	(46, 55)
$K_{d,SERCA}$	Dissociation constant for SERCA buffer	0.6 µmol/L	
$K_{d,CALM}$	Dissociation constant for Calmodulin buffer	7 µmol/L	
$K_{d,phosphoL}$	Dissociation constant for phospholipid (low) buffer	13 µmol/L	
$K_{d,phosphoH}$	Dissociation constant for phospholipid (high) buffer	0.3 µmol/L	
$K_{d,myosin}$	Dissociation constant for myosin buffer	4.62 µmol/L	
$K_{d,ATP}$	Dissociation constant for ATP buffer	1200 µmol/L	
$K_{d,FLUO}$	Dissociation constant for Fluo-4 buffer	0.739 µmol/L	
Ca^{2+} diffusion constants			
D_{sub}	Subsarcolemmal Ca^{2+} diffusion constant	$7.8*10^{-10}$ m²/s	(55)
D_{cyto}	Cytoplasmic Ca^{2+} diffusion constant	$3.5*10^{-10}$ m²/s	(56)
Cx43 hemichannel parameters			
I_{Ca}	Hemichannel mediated Ca^{2+} current	0-3 pA	Estimate
$T_{o,\ HC}$	Open time hemichannel	8.16 ms	Experiment

Na^+/Ca^{2+} exchanger parameters			
g_{NCX}	NCX conductance	52.5 µmol/L/ms	(49, 52)
$K_{m,Cai}$	Dissociation constant for intracellular Ca^{2+}	0.00359 mmol/L	
$K_{m,Cao}$	Dissociation constant for extracellular Ca^{2+}	1.3 mmol/L	
$K_{m,Nai}$	Dissociation constant for intracellular Na^+	12.3 mmol/L	
$K_{m,Nao}$	Dissociation constant for extracellular Na^+	87.5 mmol/L	
k_{sat}	Maximal NCX turnover	0.27	
n_{Hill}	Hill coefficient	3	
K_{mCaAct}	Ca^{2+} activation constant	150 nmol/L	(57)
ε	NCX voltage dependence coefficient	0.35	
Ryanodine receptor parameters			
I_{RyR}	RyR current	0.35 pA	(53, 58)
k_{on}	RyR on rate	$1.25*10^8$ mol/L^{-1} s^{-1}	
k_{off}	RyR off rate	75 s^{-1}	
β_{PN}	Number of RyRs in supercluster at perinexus	155	Experiment
β_{myo}	Number of RyRs in supercluster at the sarcomeres	111	

Supplemental Table 5. *Modeling parameters, experimental values are obtained in mouse*

Monophasic action potential recording

Left ventricular (LV) tissue wedges (2-5 cm^2) were prepared by cannulating a distal LV coronary artery and dissecting its perfusing territory, any arterial leaks were sutured. The wedge was then mounted in a modified Langendorff-perfusion system and perfused with oxygenated Tyrode's solution at 37 ± 1°C with a constant flow rate of ~5 mL/min. The wedge was fully submerged in an oxygenated Tyrode's-filled chamber maintained at 37 ± 1°C. Modified silver chloride bipolar electrodes (0.5 mm diameter), positioned transmurally at the edges of the LV wedge, were used to record a pseudo-electrocardiogram (ECG). A standard 2 mm quadripolar electrophysiology (EP) catheter (Biosense Webster, Belgium) was positioned on the endocardial surface of the wedge for pacing. A monophasic action potential (MAP) catheter (MedFact

Engineering GmbH, Germany) was used to record the MAPs from the mid-myocardial layer of the LV wedge. All signals were filtered between 0.01 Hz - 1 kHz, digitized at 4 kHz and recorded using a LABSYSTEM PRO EP recording system (Boston Scientific, USA). All recordings were only performed after a stabilization period of 10-20 minutes, when the LV wedges were quiescent.

Baseline MAPs and ECG were recorded for 5 minutes with endocardial pacing at 1 Hz by a square pulse of 2-5 ms and intensity adjusted according to supra-capture threshold 2-10 V. A conditioning 2 minutes pacing train at 1 Hz and 2 Hz was then applied, followed by a rest 'diastolic' phase for 1 minute to observe spontaneous activity. Thereafter, pharmacological intervention (TAT-Gap19 80 µmol/L) or vehicle were added to the perfusing Tyrode's solution for 10 minutes while pacing at 1 Hz. Then isoproterenol (ISO) 100 nmol/L was added to the perfusate, and the conditioning 1 Hz and 2 Hz pacing protocol was repeated for 2 minutes, with 1 minute diastolic rest thereafter to observe spontaneous activity.

Statistical analysis

Data are expressed as mean ± standard error of the mean (SEM) unless otherwise indicated, with 'n' denoting the number of cells and 'N' denoting the number of independent experiments. Following outlier analysis (mean ± 3xSD), normality of distribution was tested and appropriate statistical test was determined for comparative statistics. Data were compared using a nested design taking into account n cells and N animals or N human hearts. A two-tailed P value < 0.05 was considered as indicating statistical significance. In the graphs, the actual P values are

provided. Statistical analysis and graphical data representation was done with Graphpad Prism (v.9).

Supplemental Tables

Unitary current properties (mean ± SEM)		
Parameter	*Mouse*	*Pig*
N_{hearts}	90	20
n_{cells}	281	55
Total number of events	9038	503
Event probability	0.051 ± 0.003	0.013 ± 0.003***
Number of events per cell	32.19 ± 2.88	3.47 ± 0.44***
Availability (%)	96.09	60
Active event probability	0.053 ± 0.003	0.021 ± 0.005**
Number of events per active cell	38.22 ± 5.35	6.31 ± 1.08
γ (pS)	227.25 ± 6.69	233.83 ± 2.36
γ_{sub} (pS)	105.81 ± 1.65	105.45 ± 3.51
Level 2 conductance (pS)	417.62 ± 32.81	442.46 ± 2.87
Level 3 conductance (pS)	620.43 ± 22.43	
Level 4 conductance (pS)	841.09 ± 10.05	
Slope γ (pS)	217.1 ± 7.49	219.6 ± 9.15
$\tau_{first\ latency}$ (ms)	94.95 ± 5	85.48 ± 10
τ_{open} (ms)	8.16 ± 0.08	8.21 ± 0.35

Supplemental Table 6. Caffeine-provoked channel properties in mouse and pig left ventricular cardiomyocytes at -70 mV (excluding slope conductance) and 37°C. γ = unitary conductance, τ = time constant. Data are presented as mean ± SEM. Significant interspecies differences are indicated with *.

Single-channel properties (mean ± SEM or range)		
Parameter	*Macropatch (cell end/ID)*	*SICM-patch*
N_{hearts}	20	5
$n_{patches}$	80/80	35
Availability (%)	32/33	12
Total number of events	370/500	32
P_o (x 10^{-3})	0.62 ± 0.42/1.75 ± 0.47	0.25 ± 0.8
Number of channels per active patch	1-2/1-2	1-2
γ (pS)	207.45 ± 1.26/210.1 ± 0.36	221.29 ± 1.05
γ_{sub} (pS)	121.46 ± 3.43/114.92 ± 0.54	113.29 ± 1.71
Level 2 conductance (pS)	423.13 ± 13.95/410.33 ± 2.11	442.46 ± 2.87
Slope γ (pS)	217.6 ± 4.41/218.2 ± 8.71	
τ_{open} (ms)	10.19 ± 0.1/15.8 ± 0.5	7.21 ± 0.75
Estimated number of channels per cell	82	204

Supplemental Table 7. Caffeine-provoked single-channel properties in mouse left ventricular cardiomyocytes during macropatch and SICM-patch recording at -70 mV (excluding slop conductance) and 37°C. P_o = open probability, γ = unitary conductance, τ = time constant. Data are presented as mean ± SEM (including ranges where applicable).

Parameter	**HF Group**
Diagnosis (N)	6 ICM, 8 DCM
Age (years)	51.92 ± 15.44
Gender	8 Male, 6 Female
BMI	26.94 ± 5.19
LVEF (%)	21.57 ± 12.06
IVSd (mm)	11.32 ± 7.68
LVPWd (mm)	12.14 ± 9.79
LVIDd (mm)	58.87 ± 15.14
LVIDs (mm)	49.83 ± 14.64
NT-pro-BNP (ng/L)	3272.71 ± 3396.1
Device (N)	7 ICD, 4 CRT-D, 6 LVAD (Heartware, Heartmate II)
Medication (N)	Platelet inhibitors/anticoagulation (14) β-blocker (13) ACE-inhibitor/ATII receptor blocker (11) Diuretics (9) PPI (9) Hormonal therapy (5) Psychotropic drugs (4) Statin (4) Anti-arrhythmic drugs (3) Antibiotics (2) Vasodilator (2) Metformin and other oral antidiabetics (2) Digoxin (2) Corticosteroids (1) Dietary supplements (e.g. iron) (1)
	NF group
Age (years)	65.88 ± 11.98
Gender	14 Male, 12 Female
BMI	25.88 ± 5.29
Heart frequency (bpm)	78.95 ± 21.14
SBP (mm Hg)	124.25 ± 20.91
DBP (mm Hg)	61.83 ± 13.18
Medication (N)	Vasopressors (18) Antibiotics (13) Corticosteroids (12) Desmopressin (8) Platelet inhibitors/anticoagulation (7) PPI (4) Vitamin supplements (4) Psychotropic drugs (4) ACE-inhibitor/ATII receptor blocker (3) α1-blocker (2) Anticonvulsants (2) β-blocker (2) Diuretics (2) Statins (2) Hormonal therapy (2)

	Insulin (2) Statin (2) Nitrates (1) Ca^{2+} antagonist (1) H1-antagonist (1)
ECG (when available)	Normal sinus rhythm (7) Sinus tachycardia (1)
Echocardiography (when available)	Normal LV and RV structure and function, no significant valvular disease (8)
Coronary angiography (when available)	No significant coronary artery disease (3)

598 **Supplemental Table 8.** Patient characteristics. Data expressed as categorical or
599 continuous (mean ± SD) variables.
600

Supplemental Figures

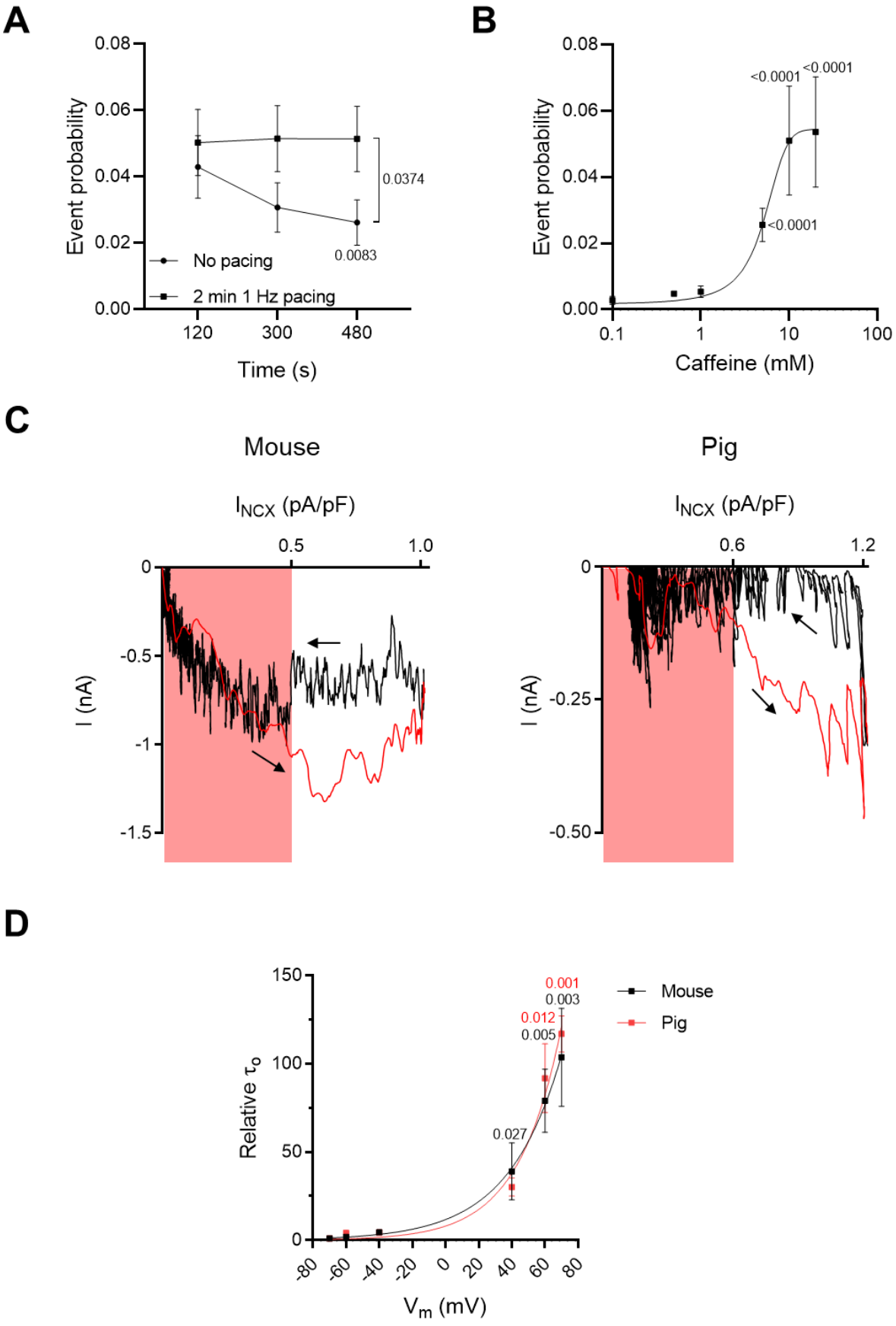

Supplemental Figure 2. Caffeine-induced Ca^{2+} release from the sarcoplasmic reticulum activates Cx43 hemichannels at resting membrane potentials: **additional validation and electrophysiological analysis.**

(A) Exposure to a 2 min pacing period at 1 Hz prevents channel rundown during the recording. Summary dot plot showing unitary current event probability during 3 caffeine applications (10 mM, 8 seconds) separated by 2 minutes of voltage clamp at resting membrane potential (dots) or pacing at 1 Hz (squares). Data obtained in freshly single mouse left ventricular cardiomyocytes (nested one-way ANOVA; N/n = 5/25).

(B) Caffeine dose-response curve showing caffeine-induced unitary current event probability (EC50 = 5.08 mmol/L). Data obtained in freshly single mouse left ventricular cardiomyocytes (N/n = 5/19). P-values compare to 0.1 mM caffeine (nested one-way ANOVA).

(C) Phase-plane plots of ensemble Cx43 hemichannel current vs NCX current (as measure of local, subsarcolemmal Ca^{2+}). Red indicates good correlation between hemichannel current and subsarcolemmal Ca^{2+} changes (N/n_{mouse} = 90/281, N/n_{pig} = 20/55).

(D) Membrane depolarization significantly increases hemichannel open duration. Data obtained in single mouse and pig left ventricular cardiomyocytes (N/n_{mouse} = 5/20, N/n_{pig} = 5/15). P-values compare to -70 mV (nested one-way ANOVA).

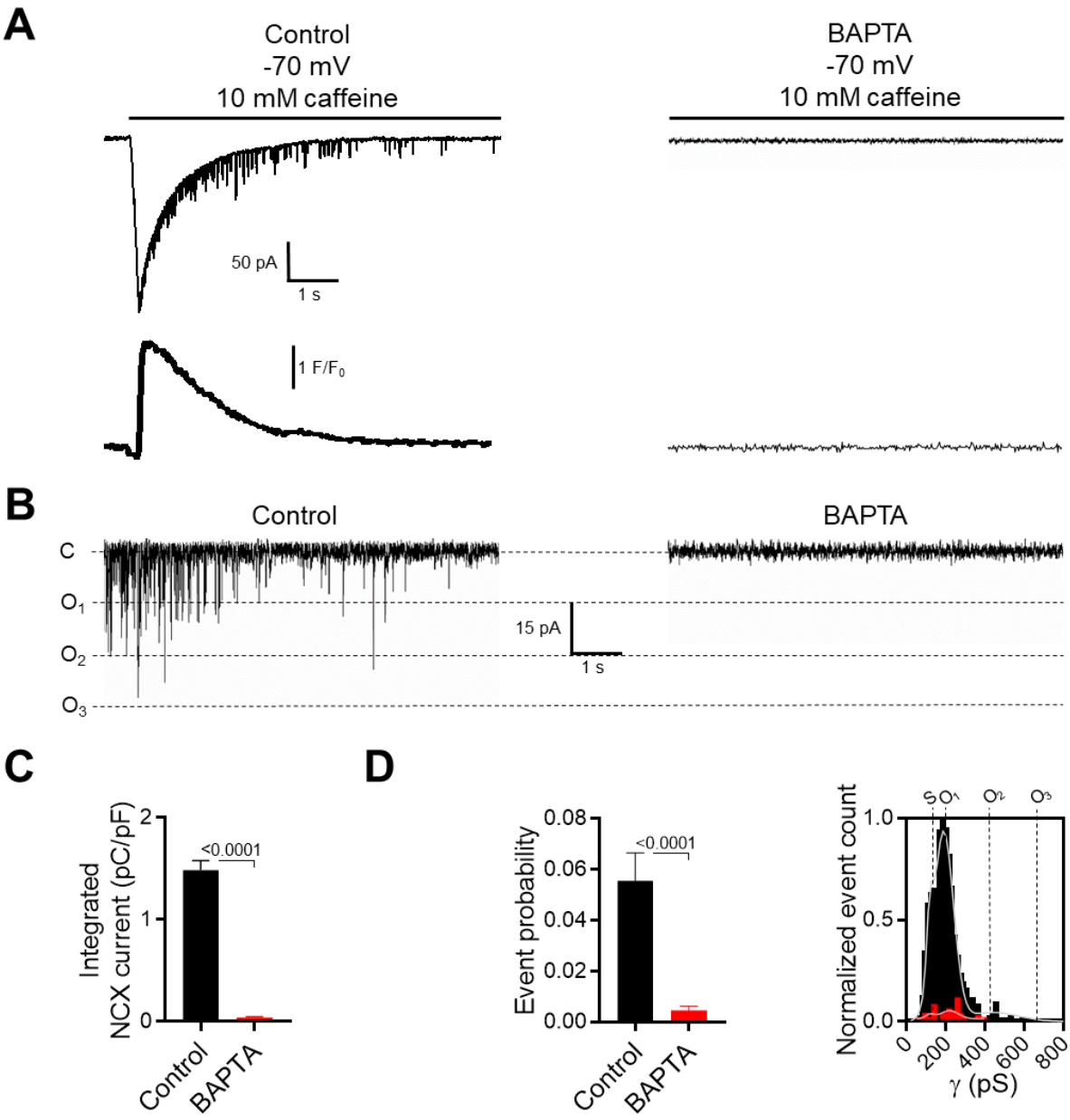

Supplemental Figure 3. Ca^{2+} release induced unitary currents are abolished by BAPTA.
(A) Example traces illustrating current and fluorescence signals during 10 mM caffeine application in single mouse cardiomyocytes voltage clamped at -70 mV during control conditions and when 10 mM BAPTA was included in the pipette.
(B) Unitary current example traces in control and in the presence of BAPTA (NCX currents subtracted).
(C) Summary graph indicating significantly reduced SR Ca^{2+} content when BAPTA was present as compared to control (nested t-test; N/n_{mouse} = 5/13).
(D) Summary bar chart and transition histogram showing significantly reduced unitary current event probability when BAPTA was present as compared to control (nested t-test; N/n_{mouse} = 5/13).

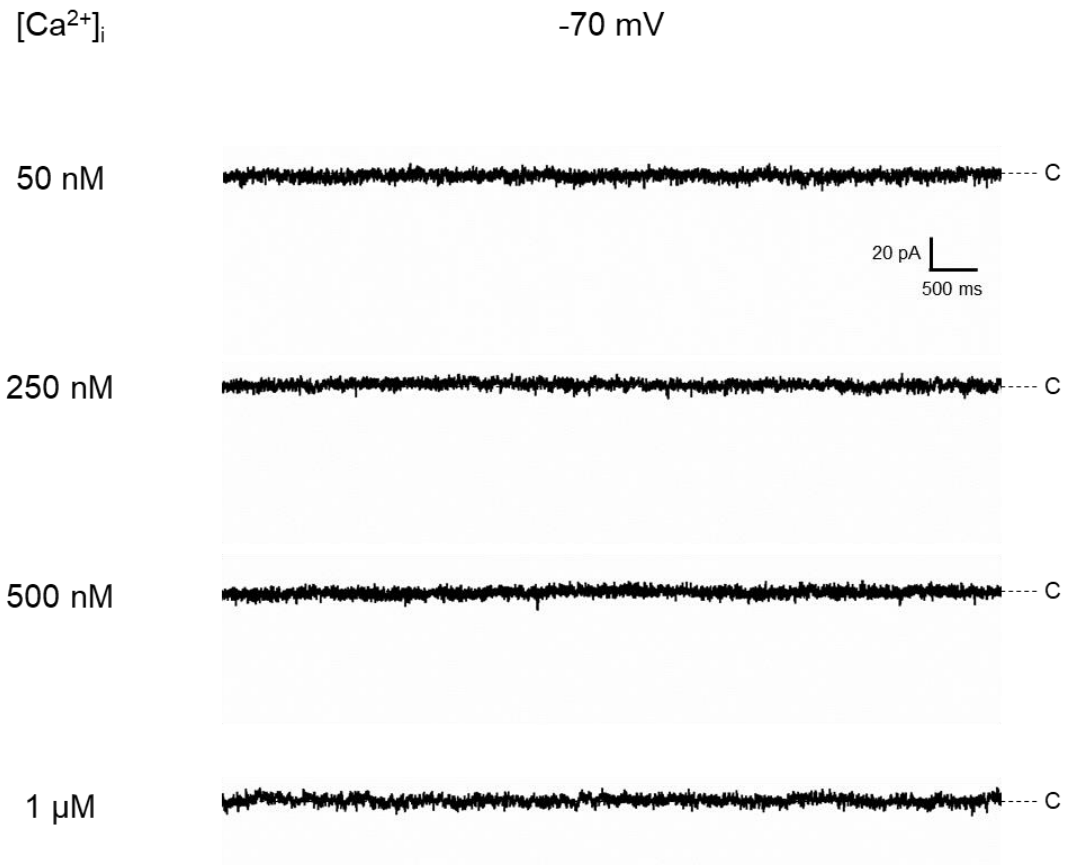

Supplemental Figure 4. Imposing stably buffered $[Ca^{2+}]_i$ elevation through the patch pipette without caffeine does not induce unitary currents.
Example traces illustrating current signals in single mouse cardiomyocytes voltage clamped at -70 mV at different levels of $[Ca^{2+}]_i$ (50, 250, 500 and 1000 nM).

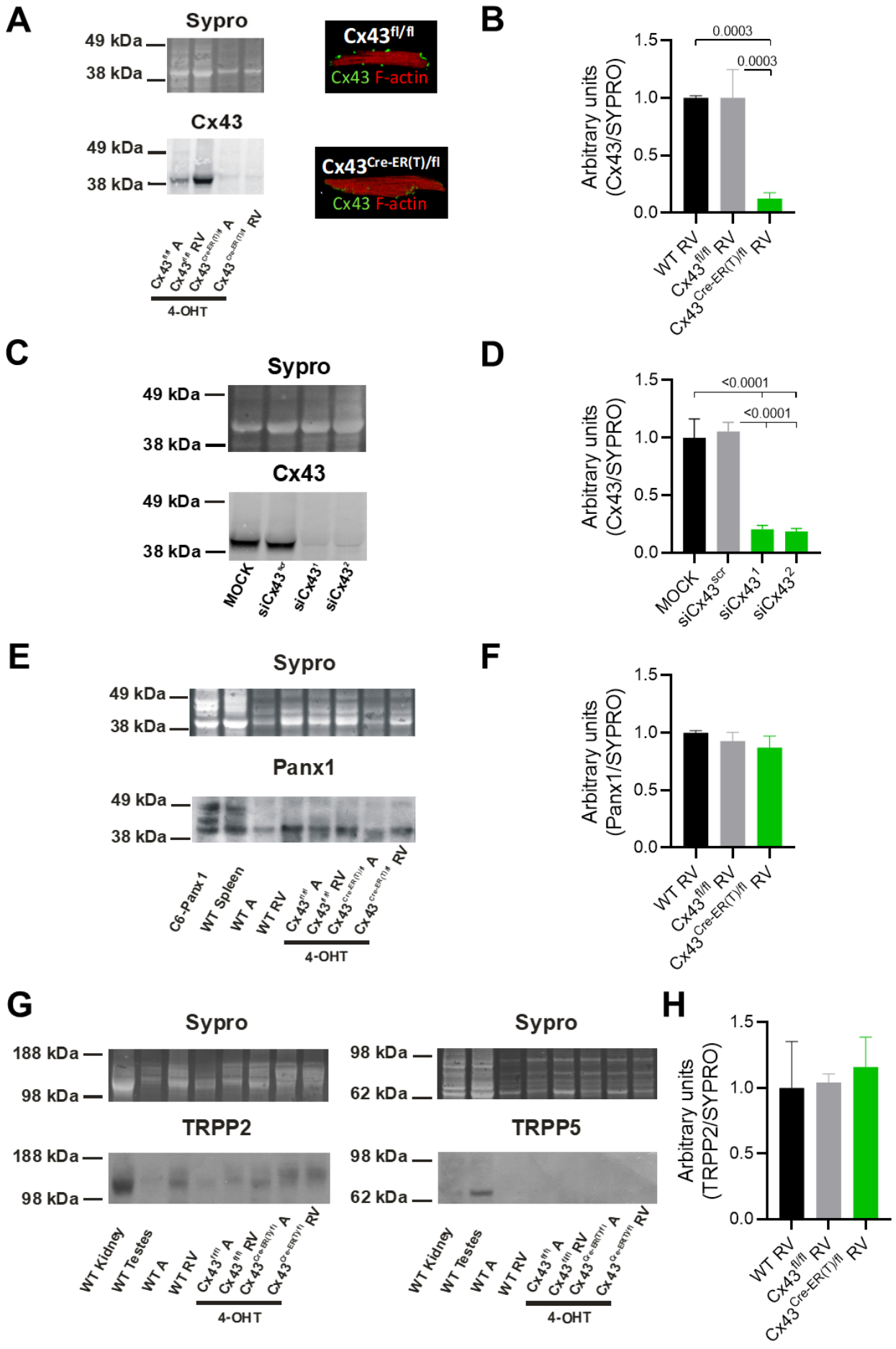
A
Sypro
49 kDa
38 kDa
Cx43
49 kDa
38 kDa
Cx43 A
Cx43 RV
Cx43 A
Cx43 RV
4-OHT
Cx43fl/fl
Cx43 F-actin
Cx43Cre-ER(T)/fl
Cx43 F-actin
B
Arbitrary units (Cx43/SYPRO)
0.0003
0.0003
1.5
1.0
0.5
0.0
WT RV
Cx43fl/fl RV
Cx43Cre-ER(T)/fl RV
C
Sypro
49 kDa
38 kDa
Cx43
49 kDa
38 kDa
MOCK
siCx43Scr
siCx43-1
siCx43-2
D
Arbitrary units (Cx43/SYPRO)
<0.0001
<0.0001
1.5
1.0
0.5
0.0
MOCK
siCx43Scr
siCx43-1
siCx43-2
E
Sypro
49 kDa
38 kDa
Panx1
49 kDa
38 kDa
C6-Panx1
WT Spleen
WT A
WT RV
Cx43fl/fl A
Cx43fl/fl RV
Cx43Cre-ER(T)/fl A
Cx43Cre-ER(T)/fl RV
4-OHT
F
Arbitrary units (Panx1/SYPRO)
1.5
1.0
0.5
0.0
WT RV
Cx43fl/fl RV
Cx43Cre-ER(T)/fl RV
G
Sypro
188 kDa
98 kDa
TRPP2
188 kDa
98 kDa
WT Kidney
WT Testes
WT A
WT RV
Cx43fl/fl A
Cx43fl/fl RV
Cx43Cre-ER(T)/fl A
Cx43Cre-ER(T)/fl RV
4-OHT
Sypro
98 kDa
62 kDa
TRPP5
98 kDa
62 kDa
WT Kidney
WT Testes
WT A
WT RV
Cx43fl/fl A
Cx43fl/fl RV
Cx43Cre-ER(T)/fl A
Cx43Cre-ER(T)/fl RV
4-OHT
H
Arbitrary units (TRPP2/SYPRO)
1.5
1.0
0.5
0.0
WT RV
Cx43fl/fl RV
Cx43Cre-ER(T)/fl RV

Supplemental Figure 5. Validation of genetic tools.

(A) Left, western blot of Cx43 protein levels in atrial and ventricular samples isolated from tamoxifen treated $Cx43^{fl/fl}$ and $Cx43^{Cre\text{-}ER(T)/fl}$ mice. Total protein quantification using SYPRO stain was used as loading control for relative quantification. Right, confocal micrographs of single mouse left ventricular cardiomyocytes double stained for Cx43 (green) and F-actin (red).

(B) Quantification of Cx43 protein levels relative to SYPRO stain (N = 5-8 per condition, 3 technical repeats, nested one-way ANOVA).

(C) Western blot of Cx43 protein levels in cultured single left ventricular pig cardiomyocytes MOCK transfected or transfected with (scrambled) Cx43 siRNA.

(D) Quantification of Cx43 protein levels relative to SYPRO stain (N = 5 per condition, 3 technical repeats, nested one-way ANOVA).

(E) Western blot of Panx1 protein levels in atrial and ventricular samples isolated from wild type, tamoxifen treated $Cx43^{fl/fl}$ and $Cx43^{Cre\text{-}ER(T)/fl}$ mice. C6-Panx1 cells and mouse spleen were used as positive controls.

(F) Quantification of Panx1 protein levels relative to SYPRO stain (N = 5 per condition, 3 technical repeats, nested one-way ANOVA).

(G) Western blots of TRPP2 (left) and TRPP5 (right) protein levels in atrial and ventricular samples isolated from wild type, tamoxifen treated $Cx43^{fl/fl}$ and $Cx43^{Cre\text{-}ER(T)/fl}$ mice. Mouse kidney and testes were used as positive controls.

(H) Quantification of TRPP2 protein levels relative to SYPRO stain (N = 5 per condition, 3 technical repeats, nested one-way ANOVA).

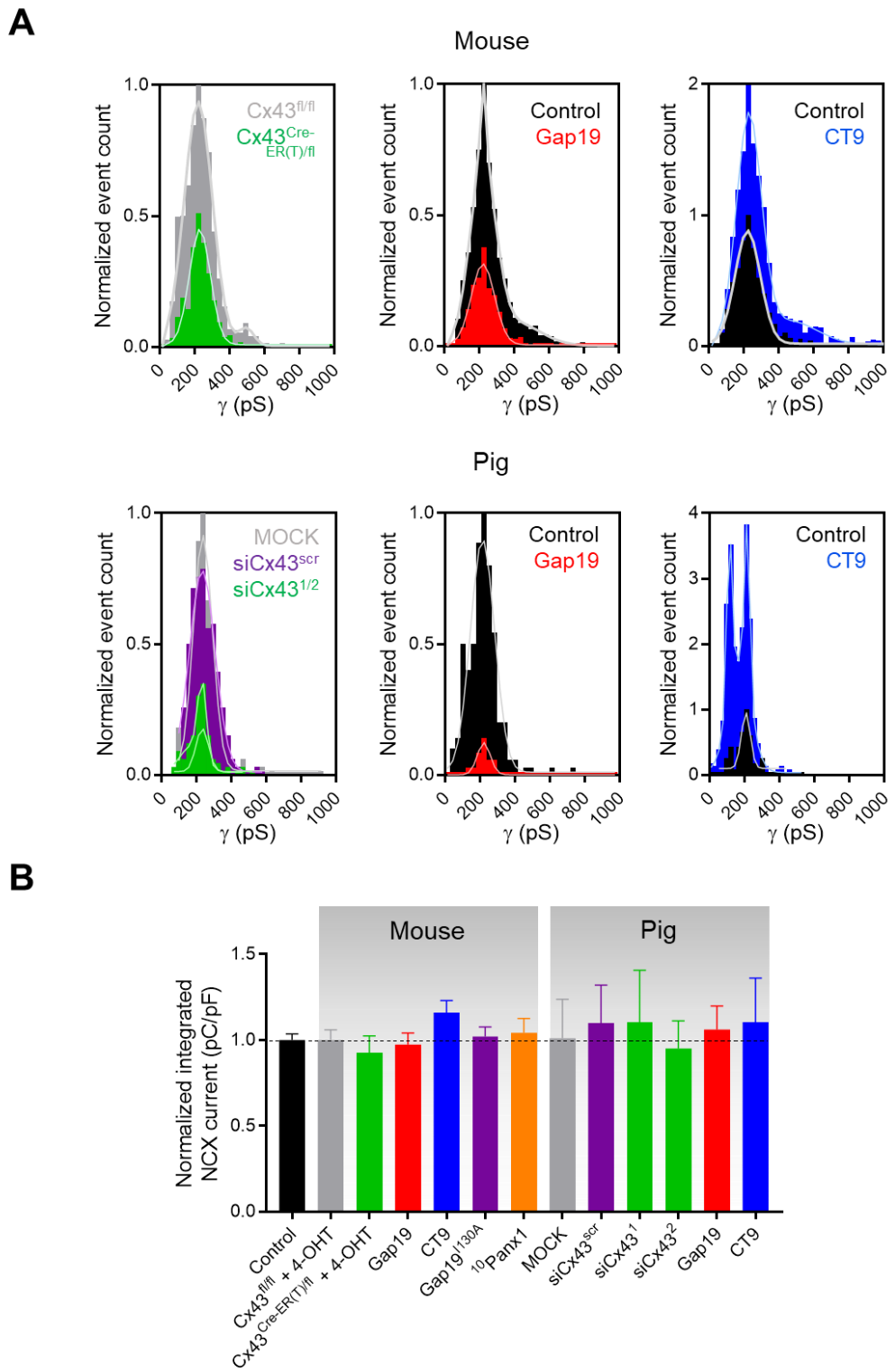

Supplemental Figure 6. Validation of peptide toolkit.
(A) Transition histograms illustrating ~220 pS caffeine-induced unitary current activities in mouse and pig single left ventricular cardiomyocytes. Statistically significant interventions and their respective control conditions from Figure 1I are shown (N/n_{mouse} = 5-16/20-49 per condition, N/n_{pig} = 5-6/15-21 per condition). (B) Summary bar chart showing SR Ca^{2+} content as measured by integrating caffeine-induced NCX current (N/n_{mouse} = 5-16/20-49 per condition, N/n_{pig} = 5-6/15-21 per condition; nested one-way ANOVA).

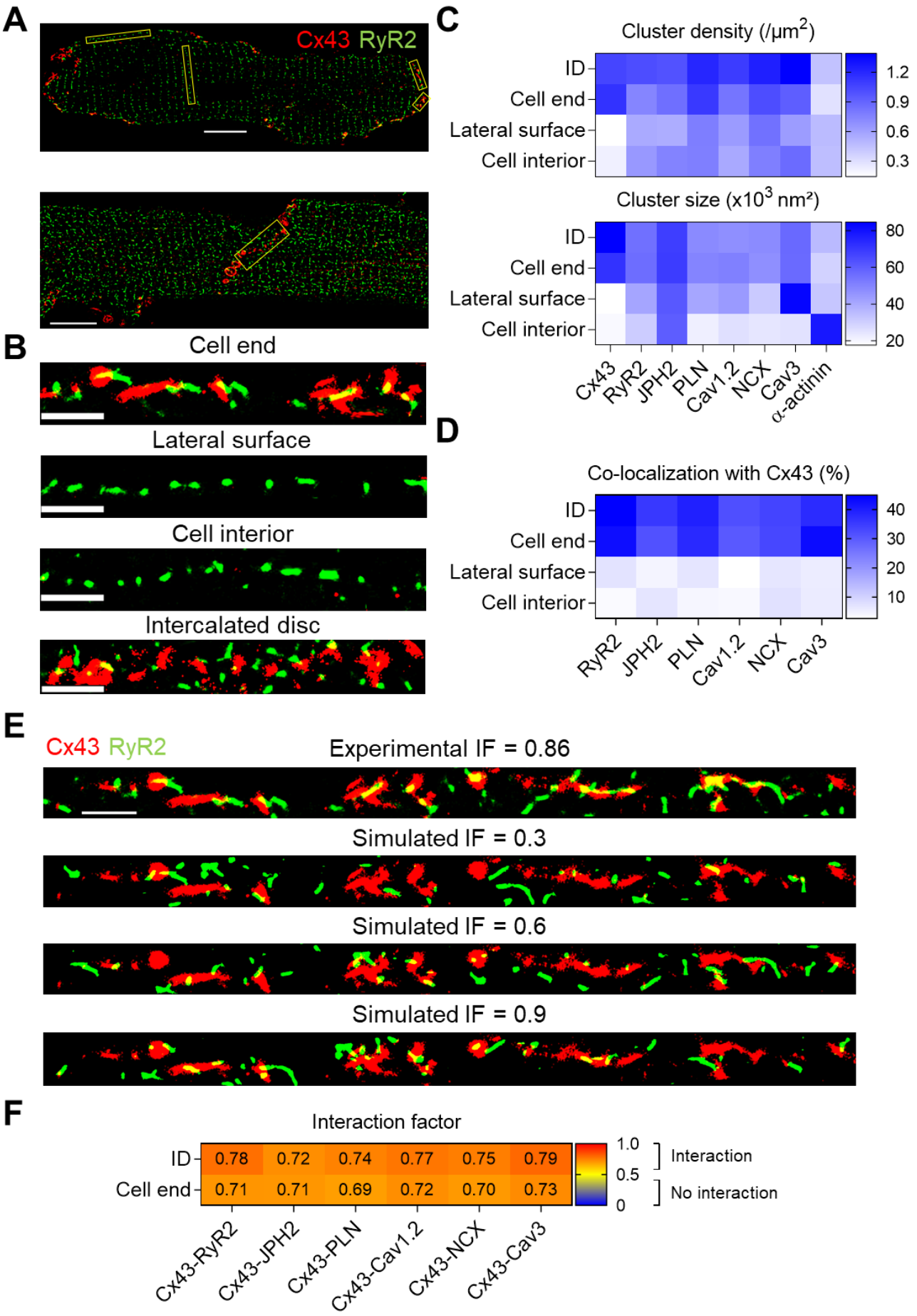
A
Cx43 RyR2
B
Cell end
Lateral surface
Cell interior
Intercalated disc
C
Cluster density (/μm²)
ID
Cell end
Lateral surface
Cell interior
1.2
0.9
0.6
0.3
Cluster size (x10³ nm²)
80
60
40
20
Cx43
RyR2
JPH2
PLN
Cav1.2
NCX
Cav3
α-actinin
D
Co-localization with Cx43 (%)
40
30
20
10
RyR2
JPH2
PLN
Cav1.2
NCX
Cav3
E
Cx43 RyR2
Experimental IF = 0.86
Simulated IF = 0.3
Simulated IF = 0.6
Simulated IF = 0.9
F
Interaction factor
ID
Cell end
0.78
0.72
0.74
0.77
0.75
0.79
0.71
0.71
0.69
0.72
0.70
0.73
1.0
0.5
0
Interaction
No interaction
Cx43-RyR2
Cx43-JPH2
Cx43-PLN
Cx43-Cav1.2
Cx43-NCX
Cx43-Cav3

Supplemental Figure 7. Robust association of Cx43 with molecular components of cardiac dyads and excitation-contraction coupling at the cell ends of single cardiomyocytes and intercalated disc of cardiomyocyte cell pairs.

(A) Example 2D SMLM images double labeled for Cx43 (red) and RyR2 (green). Top, image of a single left ventricular mouse cardiomyocyte. Bottom, image of a cardiomyocyte cell pair. Scale bars = 10 µm.

(B) Straightened region of interests (from yellow boxes in A) of Cx43 and RyR2 at different subcellular domains. Scale bar = 2 µm.

(C) and (D) Mean cluster density, cluster size and colocalization with Cx43 heat maps at different subcellular regions of all tested markers in double stainings (Cx43-X, N/n = 3-5/17-79 per condition)).

(E) Experimental and simulated interaction factors (IFs) from a region of interest at the cell end of a single mouse ventricular cardiomyocyte. Scale bar = 2 µm.

(F) Mean interaction factor heat map depicting the likelihood of co-localization with Cx43 (N/n = 3-5/17-79 per condition). Interaction factor > 0.6 indicates that co-localization is deterministic rather than random.

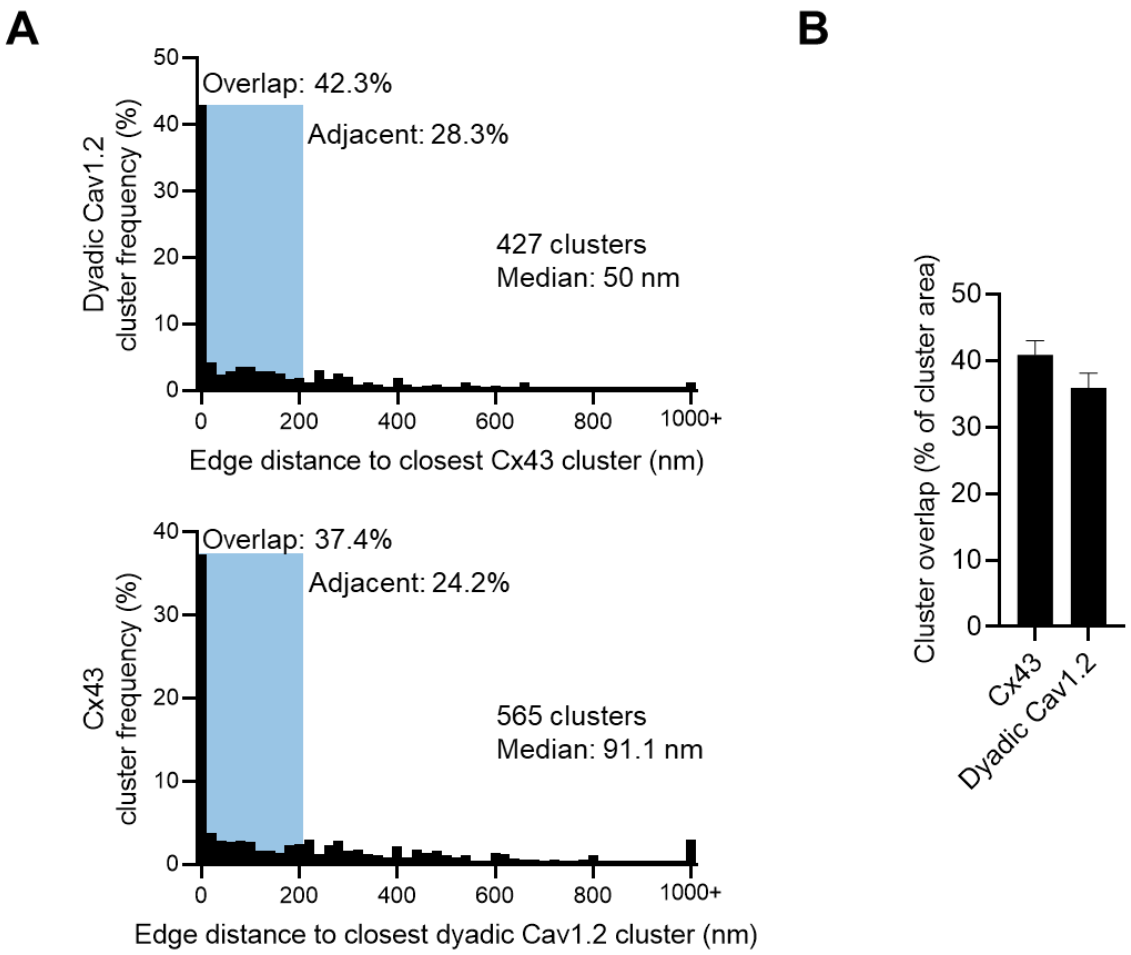

Supplemental Figure 8. Relative localization analysis of 2D triple-color SMLM images obtained in mouse left ventricular cardiomyocyte cell pairs.
(A) Summary histograms of edge distances between Cx43 and dyadic Cav1.2 (as determined by edge distance < 250 nm of RyR2 cluster) clusters (N/n = 5/16). Summation of overlapping (edge distance < 20 nm) and adjacent (edge distance 20-200 nm) clusters yields the perinexal fraction. Clusters > 200 nm yield the distant fraction.
(B) Summary graph of the degree of cluster overlap (N/n = 5/16).

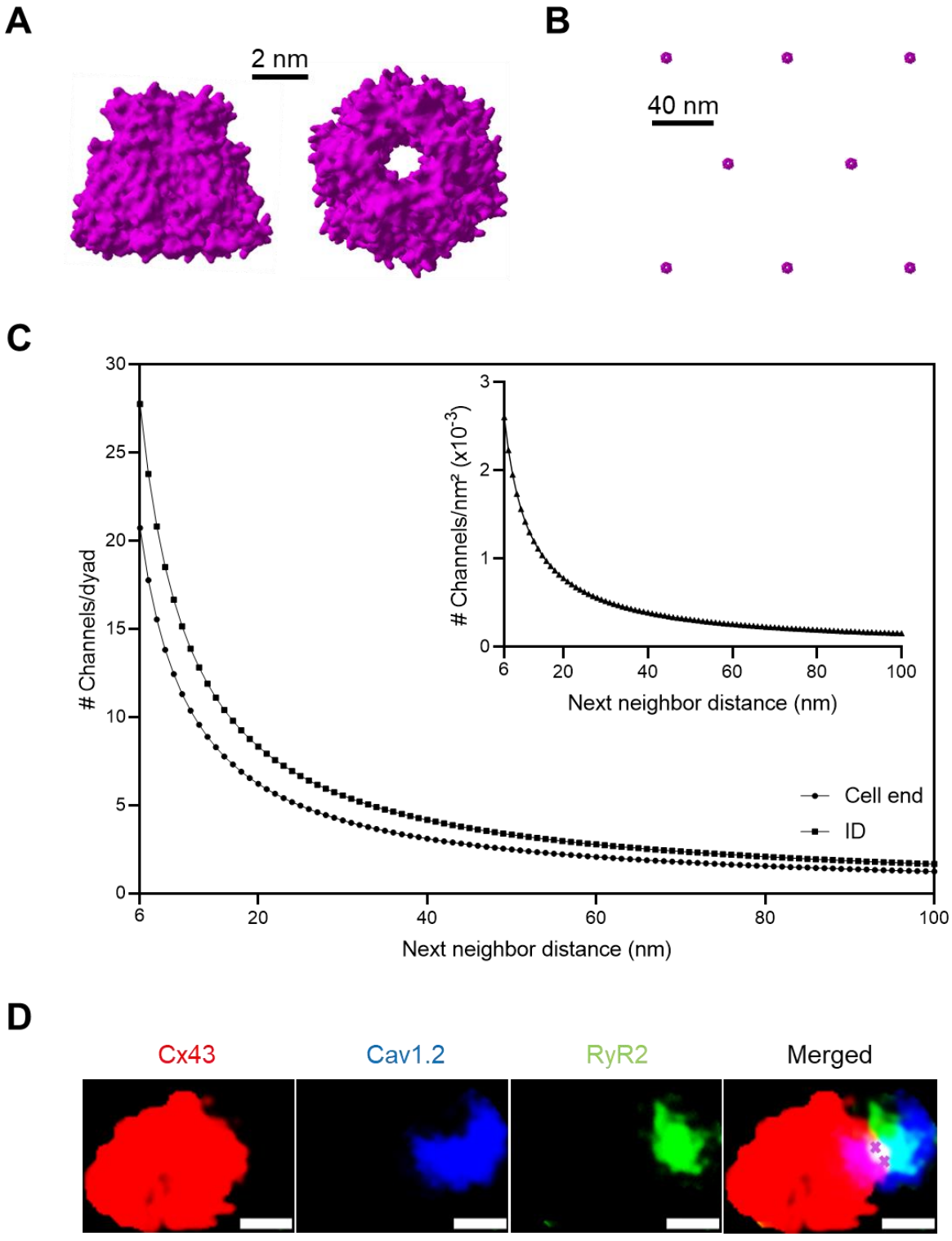

703

704 **Supplemental Figure 9. Estimation of Cx43 hemichannels per dyad using**
705 **molecular modeling.**
706 (A) 3D rendering of Cx43 hexamer generated based on monomeric murine Cx43
707 structure using SWISS-MODEL and SymmDock.
708 (B) Hexagonal array of Cx43 hexamers.
709 (C) Plots representing number of Cx43 hexamers per dyad as a function of next
710 neighbor distance. Gap junctional studies using freeze fracture electron microscopy
711 suggest a next neighbor distance of 8-10 nm between Cx43 gap junctions. In

addition, studies of the perinexus suggested that density of Cx43 hemichannels is 10 times lower than the density of gap junctions in plaques. As such, number of Cx43 hemichannels per dyad at the cell end of single cardiomyocytes or at the intercalated disc of cardiomyocyte cell pairs is suggested to be ~2.
(D) Particle averaged Cx43, Cav1.2 and RyR2 clusters. Purple crosses indicate position of Cx43 hemichannels suggested by protein modeling. Scale bar = 250 nm.

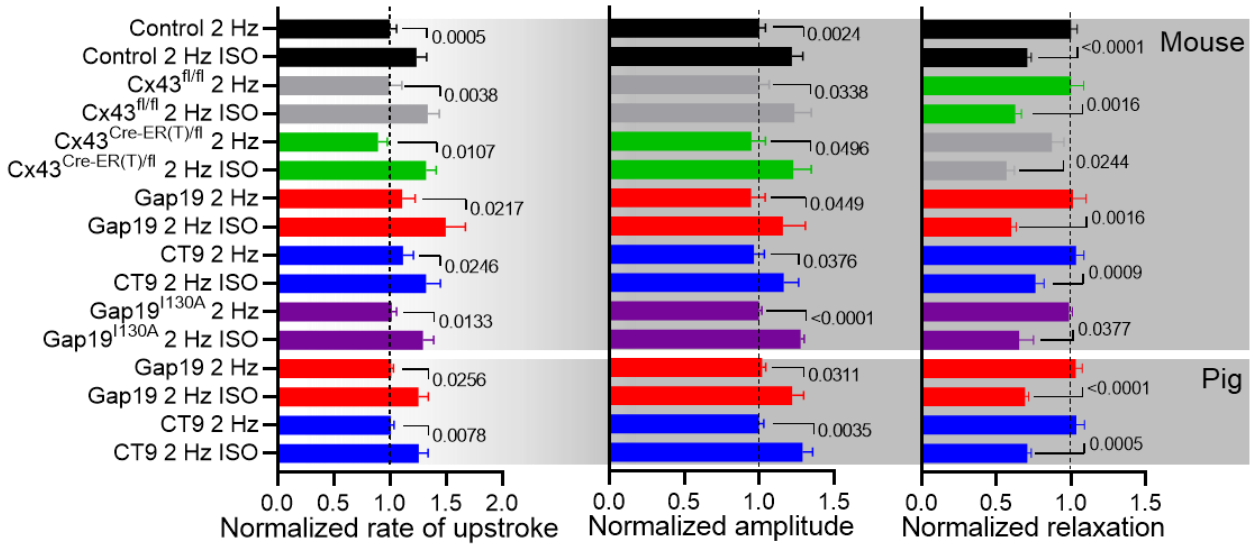

Supplemental Figure 10. Effects of Cx43 targeting peptides and Cx43 knockdown on global Ca^{2+} handling.
Ca^{2+} transient kinetics at 2 Hz pacing ± ISO and effects of Gap19, CT9 and Cx43 knockdown (nested one-way ANOVA; N/n_{mouse} = 5-11/15-24 per condition, N/n_{pig} = 5/15 per condition).

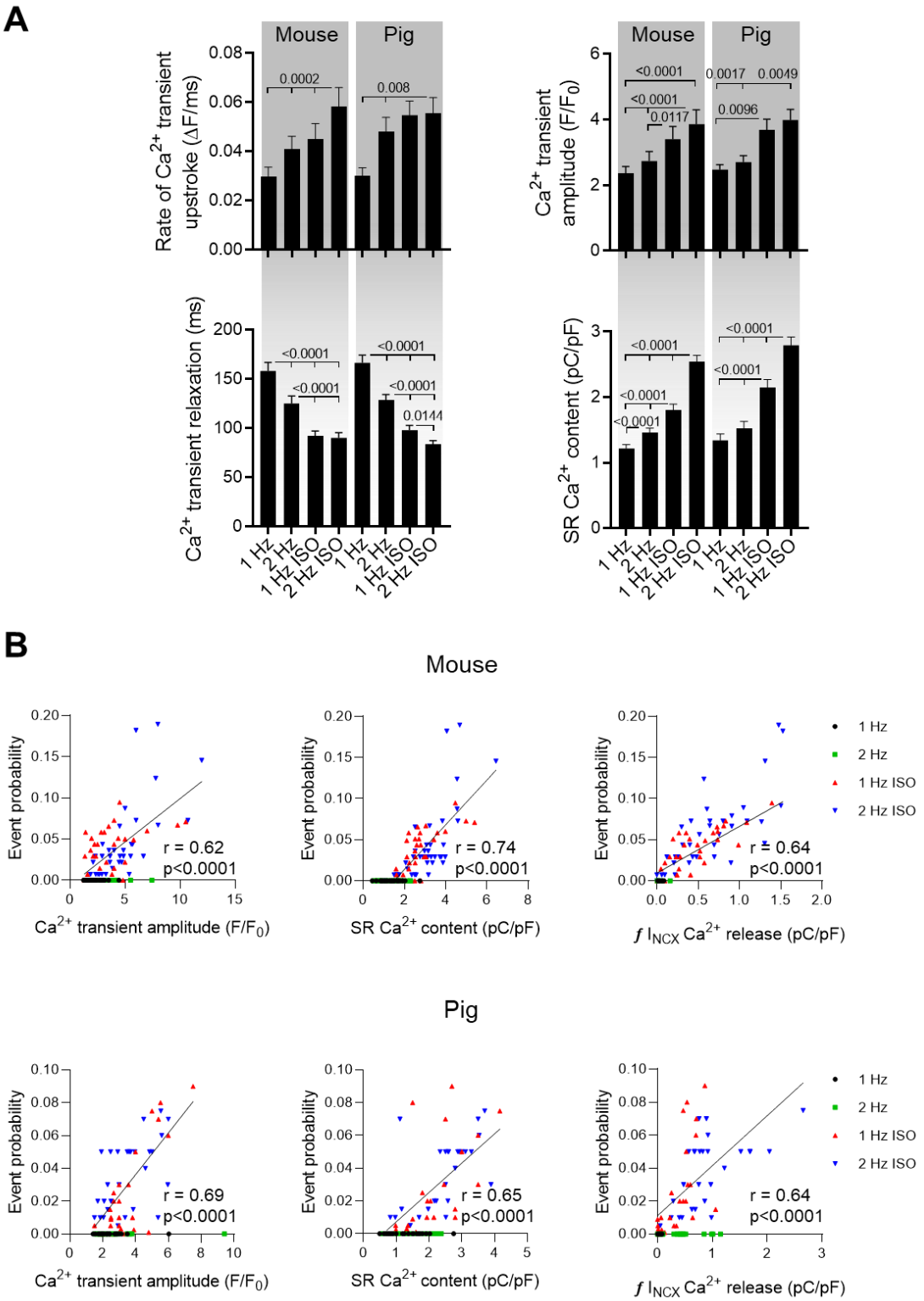

Supplemental Figure 11. Changes in global Ca^{2+} handling with adrenergic stimulation and relation to unitary current activity.

(A) Summary bar charts showing increased global Ca^{2+} handling upon adrenergic stimulation (nested one-way ANOVA; N/n_{mouse} = 23/75, N/n_{pig} = 10/30).

(B) Dot plots illustrating strong correlation between unitary current events during spontaneous Ca^{2+} release and increased intracellular Ca^{2+} during adrenergic stimulation (N/n_{mouse} = 23/75, N/n_{pig} = 10/30).

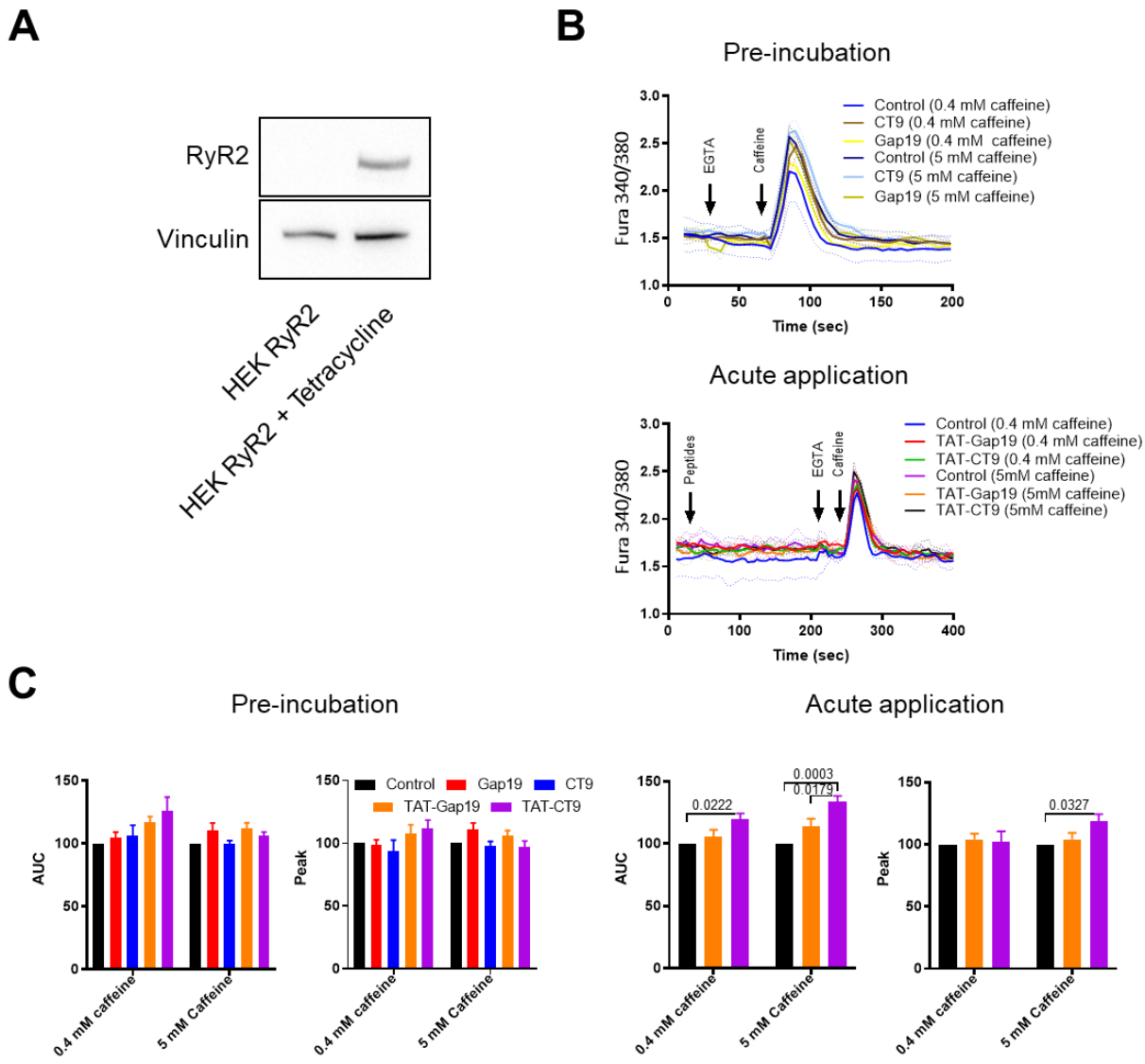

734

735 **Supplemental Figure 12. Control experiments testing the effect of Cx43**
736 **targeting peptides on RyR2 provoked Ca^{2+} changes.**
737 (A) Western blotting showing RyR2 protein expression in HEK RyR2 cell lysates
738 before and after tetracycline exposure. Vinculin was used as loading control.
739 (B) Averaged (± SEM) caffeine-induced Ca^{2+} transients under control conditions or
740 following pre-incubation or acute exposure of peptides in HEK cells overexpressing
741 RyR2 (N = 5).
742 (C) Summary bar charts of caffeine-induced Ca^{2+} transient integration (AUC) and
743 peak under control conditions, and following pre-incubation or acute exposure of
744 peptides in HEK cells overexpressing RyR2 (one-way ANOVA; N = 5).

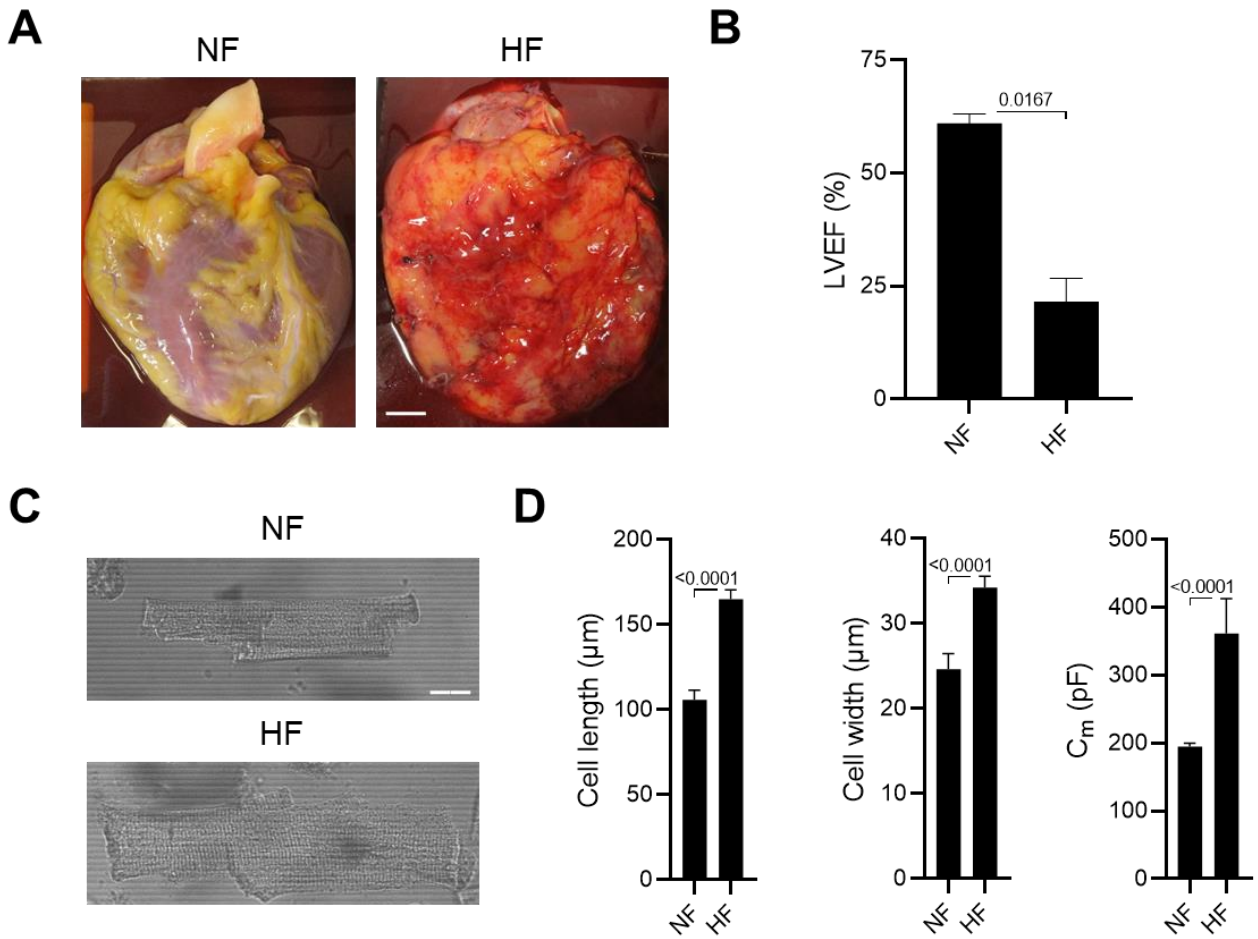

Supplemental Figure 13. Remodeling in non-failing versus failing human hearts and cardiomyocytes.

(A) Photographs of non-failing (NF, left) vs failing human heart (HF, right). Scale bar = 2 cm.

(B) Summary bar chart showing significantly decreased left ventricular ejection fraction (LVEF) in failing as compared to non-failing human hearts (nested t-test; $N_{NF/HF}$ = 3/14).

(C) Transmitted light micrographs of left ventricular cardiomyocytes isolated from non-failing (top) and failing (bottom) human hearts. Scale bar = 20 µm.

(D) Summary bar charts showing significantly increased cell length, cell width and membrane capacitance (C_m) of left ventricular cardiomyocytes isolated from human failing hearts as compared to non-failing hearts (nested t-test; $N_{NF/HF}$ = 5/5, $n_{NF/HF}$ = 24/59).

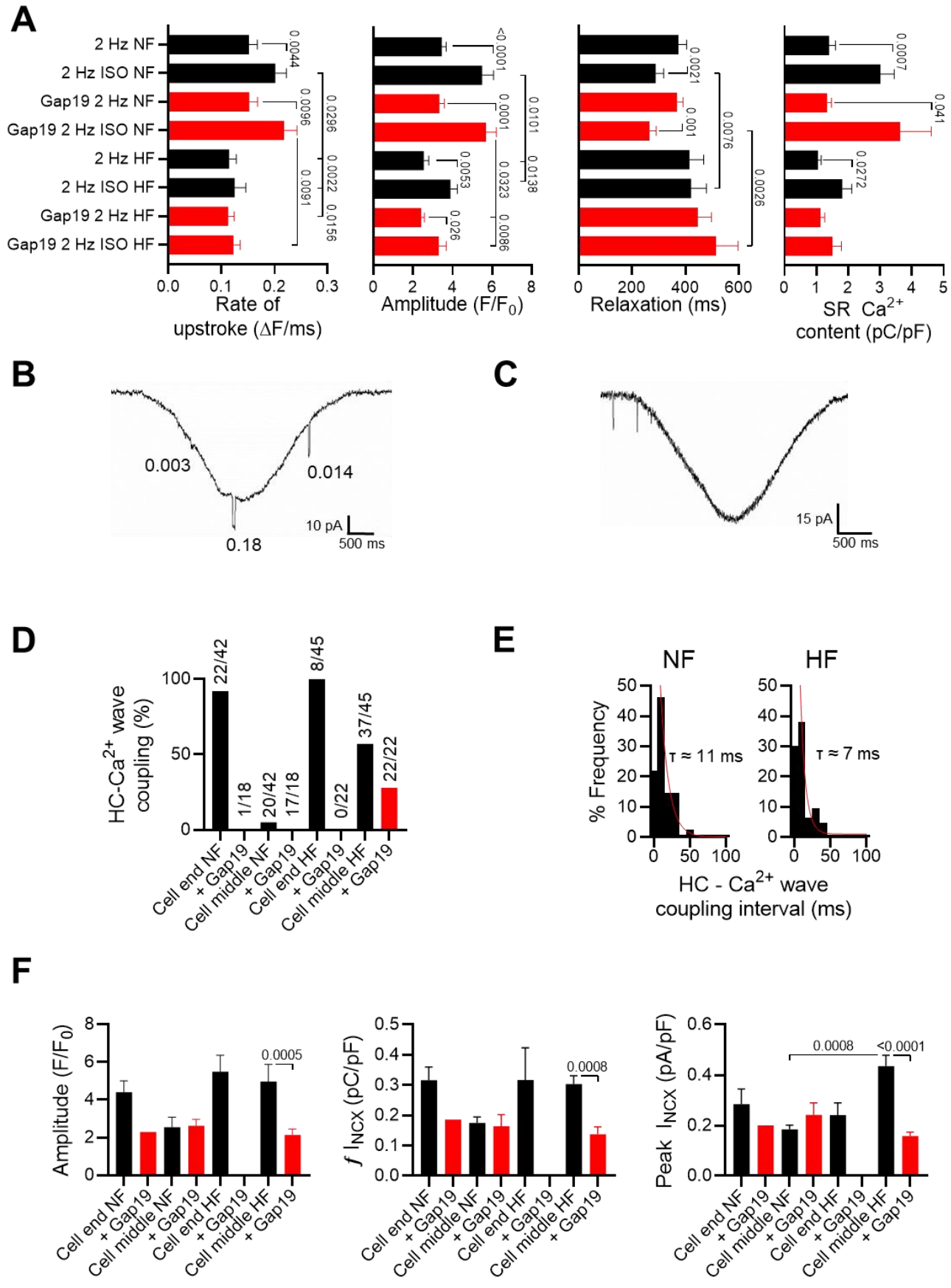
A
2 Hz NF
2 Hz ISO NF
Gap19 2 Hz NF
Gap19 2 Hz ISO NF
2 Hz HF
2 Hz ISO HF
Gap19 2 Hz HF
Gap19 2 Hz ISO HF
0.0044
0.0096
0.0296
0.0022
0.0091
0.0156
<0.0001
0.0001
0.0101
0.0053
0.0323
0.0138
0.026
0.0086
0.0021
0.001
0.0076
0.0026
0.0007
0.041
0.0272
Rate of upstroke (ΔF/ms)
Amplitude (F/F0)
Relaxation (ms)
SR Ca2+ content (pC/pF)
B
0.003
0.014
0.18
10 pA
500 ms
C
15 pA
500 ms
D
HC-Ca2+ wave coupling (%)
22/42
1/18
20/42
17/18
8/45
0/22
37/45
22/22
Cell end NF
+ Gap19
Cell middle NF
+ Gap19
Cell end HF
+ Gap19
Cell middle HF
+ Gap19
E
NF
HF
% Frequency
τ ≈ 11 ms
τ ≈ 7 ms
HC - Ca2+ wave coupling interval (ms)
F
Amplitude (F/F0)
0.0005
f INCX (pC/pF)
0.0008
Peak INCX (pA/pF)
0.0008
<0.0001

Supplemental Figure 14. Changes in global Ca^{2+} handling and hemichannel associated local Ca^{2+} signaling in human heart failure with and without Gap19.
(A) Ca^{2+} transient kinetics and SR Ca^{2+} content at 2 Hz pacing ± ISO (10 nmol/L) and effects of Gap19 in left ventricular cardiomyocytes isolated from non-failing and failing human hearts ($N_{NF/HF}$ = 5/5, $n_{NF/HF}$ = 21-23/15-17 per condition; nested one-way ANOVA).
(B) NCX current during spontaneous Ca^{2+} release with superimposed unitary current activity. Numbers indicate unitary current event probability during rising, peak and recovery phase of NCX current.
(C) Unitary current activity preceding spontaneous diastolic Ca^{2+} release.
(D) Fraction of Cx43 hemichannel (HC)-associated Ca^{2+} release in left ventricular cardiomyocytes isolated from non-failing and failing human hearts ($N_{NF/HF}$ = 5/5, $n_{NF/HF}$ = 21-23/15-17 per condition). Bar chart indicates that HC-Ca^{2+} release coupling is isolated in Ca^{2+} waves originating from the cell end in non-failing cardiomyocytes. In failing cardiomyocytes, HC-associated Ca^{2+} release originates from both the cell end and the cell middle. Gap19 abolished HC-associated Ca^{2+} release. Numbers show absolute amounts of recorded Ca^{2+} waves.
(E) Histograms indicate time from hemichannel opening to start of Ca^{2+} release for non-failing and failing human cardiomyocytes.
(F) Bar charts summarizing properties of spontaneous diastolic Ca^{2+} release and resulting NCX currents categorized based on origin in the presence or absence of Gap19 in left ventricular cardiomyocytes isolated from non-failing and failing human hearts (nested one-way ANOVA; $N_{NF/HF}$ = 5/5, $n_{NF/HF}$ = 21-23/15-17 per condition).

Supplemental Videos

Supplemental Video 1 and 2. Focused ion beam-scanning electron microscopy (FIB-SEM) three-dimensional ultrastructure from murine left ventricle: intercalated disc overview and detail at the perinexus respectively.

Supplemental Video 3 and 4. Ca^{2+} waves, recorded in murine left ventricular cardiomyocytes, originating from the cell middle and cell end respectively. White ROI indicates cell contour as determined by maximal intensity projection of fluorescence time course.

Supplemental References

1. Boengler K, Ruiz-Meana M, Gent S, Ungefug E, Soetkamp D, Miro-Casas E, et al. Mitochondrial connexin 43 impacts on respiratory complex i activity and mitochondrial oxygen consumption. *J Mol Cell Med.* 2012;16(8):1649-55.
2. Boengler K, Ungefug E, Heusch G, Leybaert L, and Schulz R. Connexin 43 impacts on mitochondrial potassium uptake. *Front Pharmacol.* 2013;4:73.
3. Eckardt D, Theis M, Degen J, Ott T, Van Rijen HVM, Kirchhoff S, et al. Functional role of connexin43 gap junction channels in adult mouse heart assessed by inducible gene deletion. *J Mol Cell Cardiol.* 2004;36(1):101-10.
4. Jansen JA, Noorman M, Musa H, Stein M, de Jong S, van der Nagel R, et al. Reduced heterogeneous expression of Cx43 results in decreased Nav1.5 expression and reduced sodium current that accounts for arrhythmia vulnerability in conditional Cx43 knockout mice. *Heart Rhythm.* 2012;9(4):600-7.
5. Jansen JA, Van Veen TAB, De Jong S, Van Der Nagel R, Van Stuijvenberg L, Driessen H, et al. Reduced Cx43 expression triggers increased fibrosis due to enhanced fibroblast activity. *Circ Arrhythm Electrophysiol.* 2012;5(2):380-90.
6. Stein M, van Veen TAB, Hauer RNW, de Bakker JMT, and van Rijen HVM. A 50% reduction of excitability but not of intercellular coupling affects conduction velocity restitution and activation delay in the mouse heart. *PLoS One.* 2011;6(6):e20310.
7. van Rijen HVM, Eckardt D, Degen J, Theis M, Ott T, Willecke K, et al. Slow conduction and enhanced anisotropy increase the propensity for ventricular tachyarrhythmias in adult mice with induced deletion of connexin43. *Circulation.* 2004;109(8):1048-55.

8. Reaume A, de Sousa P, Kulkarni S, Langille B, Zhu D, Davies T, et al. Cardiac malformation in neonatal mice lacking connexin43. *Science.* 1995;267(5205):1831-4.

9. Dries E, Bito V, Lenaerts I, Antoons G, Sipido KR, and Macquaide N. Selective modulation of coupled ryanodine receptors during microdomain activation of calcium/calmodulin-dependent kinase II in the dyadic cleft. *Circ Res.* 2013;113(11):1242-52.

10. Wang N, De Bock M, Decrock E, Bol M, Gadicherla A, Bultynck G, et al. Connexin targeting peptides as inhibitors of voltage- and intracellular Ca^{2+}-triggered Cx43 hemichannel opening. *Neuropharmacology.* 2013;75:506-16.

11. Dries E, Santiago DJ, Gilbert G, Lenaerts I, Vandenberk B, Nagaraju CK, et al. Hyperactive ryanodine receptors in human heart failure and ischaemic cardiomyopathy reside outside of couplons. *Cardiovasc Res.* 2018;114(11):1512-24.

12. Sipido KR, Stankovicova T, Flameng W, Vanhaecke J, and Verdonck F. Frequency dependence of Ca^{2+} release from the sarcoplasmic reticulum in human ventricular myocytes from end-stage heart failure. *Cardiovasc Res.* 1998;37(2):478-88.

13. Cerrone M, Lin X, Zhang M, Agullo-Pascual E, Pfenniger A, Chkourko Gusky H, et al. Missense mutations in plakophilin-2 cause sodium current deficit and associate with a brugada syndrome phenotype. *Circulation.* 2014;129(10):1092-103.

14. Lin X, Liu N, Lu J, Zhang J, Anumonwo JMB, Isom LL, et al. Subcellular heterogeneity of sodium current properties in adult cardiac ventricular myocytes. *Heart Rhythm.* 2011;8(12):1923-30.

15. Rivaud MR, Agullo-Pascual E, Lin X, Leo-Macias A, Zhang M, Rothenberg E, et al. Sodium Channel Remodeling in Subcellular Microdomains of Murine Failing Cardiomyocytes. *J Am Heart Assoc.* 2017;6(12):e007622.
16. Bhargava A, Lin X, Novak P, Mehta K, Korchev Y, Delmar M, et al. Super-resolution scanning patch clamp reveals clustering of functional ion channels in adult ventricular myocyte. *Circ Res.* 2013;112(8):1112-20.
17. Sakmann B, Neher E, eds. *Single-Channel Recording.* New York: Plenum Press; 1995.
18. Ramanan SV, and Brink PR. Multichannel recordings from membranes which contain gap junctions. II. Substates and conductance shifts. *Biophys J.* 1993;65(4):1387-95.
19. Wang HZ, Day N, Valcic M, Hsieh K, Serels S, Brink PR, et al. Intercellular communication in cultured human vascular smooth muscle cells. *Am J Physiol Cell Physiol.* 2001;281(1):C75-88.
20. Ester M, Kriegel H-P, Sander J, and Xu X. Density-Based Clustering in Spatial Databases: The Algorithm GDBSCAN and Its Applications. *Data Mining and Knowledge Discovery.* 1998;2:169-194.
21. Waterhouse A, Bertoni M, Bienert S, Studer G, Tauriello G, Gumienny R, et al. SWISS-MODEL: Homology modelling of protein structures and complexes. *Nucleic Acids Res.* 2018;46(W1):W296-W303.
22. Schneidman-Duhovny D, Inbar Y, Nussinov R, and Wolfson HJ. PatchDock and SymmDock: Servers for rigid and symmetric docking. *Nucleic Acids Res.* 2005;33:W363-7.
23. Vanslembrouck B, Kremer A, Pavie B, van Roy F, Lippens S, and van Hengel J. Three-dimensional reconstruction of the intercalated disc including the

intercellular junctions by applying volume scanning electron microscopy. *Histochem Cell Biol.* 2018;149(5):479-90.

24. Jiang D, Xiao B, Yang D, Wang R, Choi P, Zhang L, et al. RyR2 mutations linked to ventricular tachycardia and sudden death reduce the threshold for store-overload-induced Ca^{2+} release (SOICR). *Proc Natl Acad Sci U S A.* 2004;101(35):13062-7.

25. Lei CL, Clerx M, Whittaker DG, Gavaghan DJ, de Boer TP, and Mirams GR. Accounting for variability in ion current recordings using a mathematical model of artefacts in voltage-clamp experiments. *Philos Trans A Math Phys Eng Sci.* 2020;378(2173):20190348.

26. Powell T, Terrar DA, and Twist VW. Electrical properties of individual cells isolated from adult rat ventricular myocardium. *J Physiol.* 1980;302(1):131-53.

27. Šimurda J, Šimurdová M, and Švecová O. A new simple approach to estimation of membrane capacitance from current responses to voltage clamp steps. *Progr Biophys Mol Biol.* 2020;157:18-23.

28. Ypey DL, Van Meerwijk WPM, Umar S, Pijnappels DA, Schalij MJ, and Van Der Laarse A. Depolarization-induced automaticity in rat ventricular cardiomyocytes is based on the gating properties of L-type calcium and slow Kv channels. *Eur Biophys J.* 2013;42(4):241-55.

29. Zaniboni M, Cacciani F, and Groppi M. Effect of input resistance voltage-dependency on DC estimate of membrane capacitance in cardiac myocytes. *Biophys J.* 2005;89(3):2170-81.

30. Ibarra J, Morley GE, and Delmar M. Dynamics of the inward rectifier K^+ current during the action potential of guinea pig ventricular myocytes. *Biophys J.* 1991;60(6):1534-9.

31. Ten Tusscher KHWJ, Noble D, Noble PJ, and Panfilov AV. A model for human ventricular tissue. *Am J Physiol Heart Circ Physiol.* 2004;286(4):H1573-89.

32. O'Hara T, Virág L, Varró A, and Rudy Y. Simulation of the undiseased human cardiac ventricular action potential: Model formulation and experimental validation. *PLoS Comput Biol.* 2011;7(5):e1002061.

33. Frazier CJ, George EG, and Jones SW. Apparent change in ion selectivity caused by changes in intracellular K^+ during whole-cell recording. *Biophys J.* 2000;78(4):1872-80.

34. Shimomura T, Yonekawa Y, Nagura H, Tateyama M, Fujiyoshi Y, and Irie K. A native prokaryotic voltage-dependent calcium channel with a novel selectivity filter sequence. *Elife.* 2020;9:e52828.

35. Hille B. *Ion channels of excitable membranes.* Sunderland, Mass: Sinauer; 2001.

36. Atkins PW, De Paula J, Keeler J. *Atkins' Physical Chemistry.* Oxford University Press, 2018.

37. Wang HZ, and Veenstra RD. Monovalent ion selectivity sequences of the rat connexin43 gap junction channel. *J Gen Physiol.* 1997;109(4):491-507.

38. Dibb KM, Eisner DA, and Trafford AW. Regulation of systolic $[Ca^{2+}]_i$ and cellular Ca^{2+} flux balance in rat ventricular myocytes by SR Ca^{2+}, L-type Ca^{2+} current and diastolic $[Ca^{2+}]_i$. *J Physiol.* 2007;585(2):579-92.

39. Sankaranarayanan R, Kistamás K, Greensmith DJ, Venetucci LA, and Eisner DA. Systolic $[Ca^{2+}]_i$ regulates diastolic levels in rat ventricular myocytes. *J Physiol.* 2017;595(16):5545-55.

40. Sipido KR, Maes M, and Van de Werf F. Low Efficiency of Ca^{2+} Entry Through the Na^{+}-Ca^{2+} Exchanger as Trigger for Ca^{2+} Release From the Sarcoplasmic Reticulum. *Circ Res.* 1997;81(6):1034-44.

41. Cheng Y, Yu Z, Hoshijima M, Holst MJ, McCulloch AD, McCammon JA, et al. Numerical analysis of Ca^{2+} signaling in Rat Ventricular Myocytes with Realistic Transverse-Axial Tubular Geometry and Inhibited Sarcoplasmic Reticulum. *PLoS Comput Biol.* 2010;6(10):e1000972.

42. Trafford AW, Díaz ME, Sibbring GC, and Eisner DA. Modulation of CICR has no maintained effect on systolic Ca^{2+}: Simultaneous measurements of sarcoplasmic reticulum and sarcolemmal Ca^{2+} fluxes in rat ventricular myocytes. *J Physiol.* 2000;522(2):259-70.

43. Venetucci LA, Trafford AW, Díaz ME, O'Neill SC, and Eisner DA. Reducing ryanodine receptor open probability as a means to abolish spontaneous Ca^{2+} release and increase Ca^{2+} transient amplitude in adult ventricular myocytes. *Circ Res.* 2006;98(10):1299-305.

44. Sigurdson W, Ruknudin A, and Sachs F. Calcium imaging of mechanically induced fluxes in tissue-cultured chick heart: Role of stretch-activated ion channels. *Am J Physiol.* 1992;262(4);H1110-5.

45. Díaz ME, Trafford AW, and Eisner DA. The effects of exogenous calcium buffers on the systolic calcium transient in rat ventricular myocytes. *Biophys J.* 2001;80(4):1915-25.

46. Smith GL, and Eisner DA. Calcium Buffering in the Heart in Health and Disease. *Circulation.* 2019;139(20):2358-71.

47. Trafford AW, Díaz ME, and Eisner DA. A novel, rapid and reversible method to measure Ca buffering and time-course of total sarcoplasmic reticulum Ca content in cardiac ventricular myocytes. *Pflugers Arch.* 1999;437(3):501-3.

48. Trafford AW, Díaz ME, O'Neill SC, and Eisner DA. Comparison of subsarcolemmal and bulk calcium concentration during spontaneous calcium release in rat ventricular myocytes. *J Physiol.* 1995;488(3):577-86.

49. Hilgemann DW, Nicoll DA, and Philipson KD. Charge movement during Na^+ translocation by native and cloned cardiac Na^+/Ca^{2+} exchanger. *Nature.* 1991;352(6337):715-8.

50. Weber CR, Ginsburg KS, Philipson KD, Shannon TR, and Bers DM. Allosteric regulation of Na/Ca exchange current by cytosolic Ca in intact cardiac myocytes. *J Gen Physiol.* 2001;117(2):119-31.

51. Weber CR, Piacentino V, Ginsburg KS, Houser SR, and Bers DM. Na^+-Ca^{2+} exchange current and submembrane $[Ca^{2+}]$ during the cardiac action potential. *Circ Res.* 2002;90(2):182-9.

52. Zhong M, Rees CM, Terentyev D, Choi BR, Koren G, and Karma A. NCX-Mediated Subcellular Ca^{2+} Dynamics Underlying Early Afterdepolarizations in LQT2 Cardiomyocytes. *Biophys J.* 2018;115(6):1019-32.

53. Cannell MB, and Soeller C. Numerical analysis of ryanodine receptor activation by L-type channel activity in the cardiac muscle diad. *Biophys J.* 1997;73(1):112-22.

54. Tao T, O'Neill SC, Diaz ME, Li YT, Eisner DA, and Zhang H. Alternans of cardiac calcium cycling in a cluster of ryanodine receptors: A simulation study. *Am J Physiol Heart Circ Physiol.* 2008;295(2):H598-H609.

55. Michailova A, DelPrincipe F, Egger M, and Niggli E. Spatiotemporal features of Ca^{2+} buffering and diffusion in atrial cardiac myocytes with inhibited sarcoplasmic reticulum. *Biophys J.* 2002;83(6):3134-51.

56. Cannell MB, Kong CHT, Imtiaz MS, and Laver DR. Control of sarcoplasmic reticulum Ca^{2+} release by stochastic RyR gating within a 3D model of the cardiac dyad and importance of induction decay for CICR termination. *Biophys J.* 2013;104(10):2149-59.

57. Wescott AP, Jafri MS, Lederer WJ, and Williams GSB. Ryanodine receptor sensitivity governs the stability and synchrony of local calcium release during cardiac excitation-contraction coupling. *J Mol Cell Cardiol.* 2016;92:82-92.

58. Mejía-Alvarez R, Kettlun C, Ríos E, Stern M, and Fill M. Unitary Ca^{2+} current through cardiac ryanodine receptor channels under quasi-physiological ionic conditions. *J Gen Physiol.* 1999;113(2):177-86.